Title

Ultrafast vibrational dynamics of the tyrosine ring mode and its application to enkephalin insertion into phospholipid membranes as probed by two-dimensional infrared spectroscopy

Journal

The Journal of Chemical Physics, 155(3)

ISSN

0021-9606

Authors

Vinogradov, Ilya
Feng, Yuan
Kumar, SK Karthick
et al.

Publication Date

2021-07-21

DOI

10.1063/5.0054428

Peer reviewed

J. Chem. Phys. **155**, 035102 (2021). Please cite this article as DOI: 10.1063/5.0054428

Ultrafast Vibrational Dynamics of the Tyrosine Ring Mode and its Application to Enkephalin Insertion into Phospholipid Membranes as Probed by Two-Dimensional Infrared Spectroscopy

Ilya Vinogradov, Yuan Feng, S. K. Karthick Kumar, Chenxu Guo, Nina Saki Udagawa, Nien-Hui Ge*

Department of Chemistry, University of California at Irvine, Irvine, CA, 92697-2025, USA

* To whom correspondence should be addressed.
Email address: nhge@uci.edu
Phone: 949-824-1263
FAX: 949-824-8571

ABSTRACT

Enkephalins are small opioid peptides whose binding conformations are catalyzed by phospholipid membranes. Binding to opioid receptors is determined by the orientation of tyrosine and phenylalanine side chains. In this work, we investigate the effects of different charged phospholipid headgroups on the insertion of the tyrosine sidechain into a lipid bilayer using a combination of 2D IR spectroscopy, anharmonic DFT calculations, and 3rd order response function modelling. The insertion is probed by using the c.a. 1515 cm^{-1} tyrosine ring breathing mode, which we found exhibits rich vibrational dynamics on the picosecond timescale. These dynamics include rapid intramolecular vibrational energy redistribution (IVR), where some of the energy ends up in a dark state that shows up as an anharmonically shifted combination band. The waiting-time dependent 2D IR spectra also show an unusual line shape distortion that affects the extraction of the frequency-frequency correlation function (FFCF), which is the dynamic observable of interest that reflects the tyrosine side-chain's insertion into the lipid bilayer. We proposed three models to account for this distortion: a hot-states exchange model, a local environment dependent IVR model, and a coherence transfer model. A qualitative analysis of these models suggests that the local environment dependent IVR rate best explains the line shape distortion, while the coherence transfer model best reproduced the effects on the FFCF. Even with these complex dynamics, we found that the tyrosine ring mode's FFCF is qualitatively correlated with the degree of insertion expected from the different phospholipid headgroups.

I. INTRODUCTION

Vibrational labels are a ubiquitous tool for studying the local environments of many different systems, spanning from biosystems such as proteins and peptides[1-11] to energy-related systems such as ionic liquids[12,13]. In 1D IR, vibrational labels are often used to measure local electric fields via the vibrational stark effect.[3,14,15] In 2D IR, this idea is extended to measure local electric field fluctuations on picosecond timescales, thereby providing ultrafast dynamic information about their environments.[1,5] Vibrational labels have provided detailed information on peptide/protein folding events, local viscosity,[12] and lipid dynamics.[16-18]

For a vibrational label to be useful, it must satisfy the following criteria. First, the label should appear in a clear IR window, away from strongly absorbing solvent modes and solute modes that are not of interest. The label must be sensitive to its local environment and would ideally have a straightforward correlation between its environment and frequency shift.[19] For studies involving biomolecules, the label should have a sufficiently strong absorption cross-section to allow access to biologically relevant concentrations of the micromolar scale.[6,8,10,20-22] For complex biomolecules such as proteins, it should also be easy to synthetically introduce vibrational labels, which is often done so as synthetically modified amino acids.[23-27] Finally, these labels should also not significantly perturb the structure or dynamics of the protein system; that is, they should only act as probes. The last point is most readily satisfied by utilizing "intrinsic labels" on amino acid side chains that naturally occur in a peptide or protein and are sensitive to the local environment.[28-33] One example, which we have studied previously,[29] is the tyrosine ring mode at 1515-1517 cm^{-1}.[29-31,34,35]. This mode is relatively strong, very narrow, and can be distinctly observed in the IR spectra of proteins.[36,37] It has been used to report the structural changes of peptides and proteins in photoactivated [38,39], electrochemical-,[40] or thermal-induced processes.[41,42]. Solvent dependent studies revealed a linear relationship between the ring mode's linear IR linewidth and the solvent electric fields.[30]

In this paper, we further explore the sensitivity of the tyrosine ring mode to its local environment with our recent advances in noise reduction.[43,44] Although recent 2D IR studies by us and the Tucker group have demonstrated the power of using this mode as a non-perturbing probe for elucidating peptide-membrane interactions[29] and the thermal and chemical

denaturing of Trp-cage miniprotein,[30,31] the frequency-frequency correlation functions (FFCFs) in these studies were measured over a relatively small waiting-time window, up to 4 ps and 2 ps, respectively. To fully establish the relationship between 2D IR line shape, linewidth, and FFCF and the underlying molecular structure and dynamics, it is important to expand the waiting-time window and perform detailed analysis and simulations to investigate the different factors that can contribute to the waiting-time dependence. To this end, we overcome the difficulty in measuring 2D IR spectra with high signal-to-noise ratios at long waiting times by applying our new referencing scheme[43,44] that has been demonstrated to reduce noise by 10-30 times and reach the noise floor of the mid-IR signal detector.

To further test the sensitivity of the tyrosine ring mode on its local environment, we revisit the enkephalin system.[29,45] Briefly, enkephalins are endogenous opioid peptides (Figure 1 (a)) whose binding to the opioid receptors is catalyzed by a lipid membrane.[46] These peptides remain largely unfolded in buffer, adopting only transient random coil conformations.[47-49] This conformational change allows for the peptide to bind to the opioid receptor, where binding-site specificity is determined by the relative positioning and orientation of the tyrosine and phenylalanine side-chains.[50-53] For example, a synthetic enkephalin mimic is morphine, where the positioning of a phenol and phenyl ring is locked.[54,55] Marcotte et al. have shown that the conformational distribution and insertion of enkephalins can be modulated by doping a phosphatidylcholine (PC) bilayers' surface with different headgroups (Figure 1 (b)).[50] The authors suggested that the main effect comes from the bilayer packing and surface charge, where highly packed bilayers with small headgroups [Phosphatidylethanolamine (PE) and phosphatidylglycerol (PG)] and negatively charged headgroups [Phosphatidylserine (PS) and phosphatidylglycerol (PG)] cause the peptide to be less inserted. Based on previous work,[29] we hypothesize that changes in the conformational distribution will be reflected in the static inhomogeneity of the tyrosine ring mode, where surface bound peptides will show a smaller static inhomogeneity than buried peptides.

In this work, we show that the tyrosine ring mode reports, within experimental error, on its local environment when the bilayer surface is doped with 10% of a different headgroup. More importantly, we found that this sensitivity is masked by complex vibrational relaxation dynamics

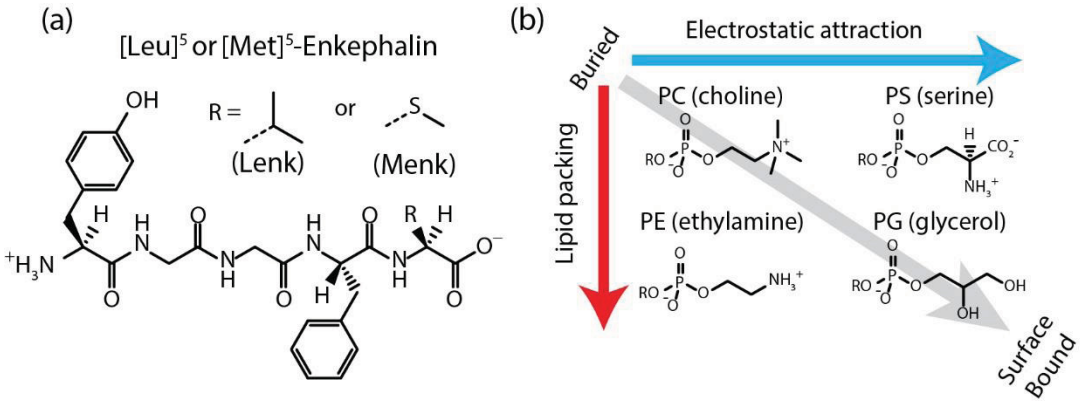

Figure 1. (a) The structure of enkephalins. (b) The expected behavior of the peptides in different bicelle conditions with different headgroup doping. Tighter lipid packing and stronger peptide-headgroup attraction would make the peptide more surface bound.

that cause a significant distortion in the 2D line shape. We propose that the ring mode undergoes efficient energy relaxation to a nearby dark-state and suggest three models to explain the spectra, two of which can explain the line shape distortion. We conclude with showing what effects these three models have on extracting the FFCF, which is the dynamic parameter of interest.

II. EXPERIMENTAL AND COMPUTATIONAL DETAILS

II.A. Sample Preparation

We followed the sample preparation protocol described previously[29] and modified by Marcotte, et al.[50] for bicelle headgroup doping. Samples were prepared to have a 25:1 lipid to peptide molar ratio. Note that even at this high ratio, peptides have been shown to be fully bound to the lipids.[56] Therefore, we did not perform a concentration dependent study to test for peptide aggregation. Briefly, lipid mixtures were prepared by mixing 1,2-dihexanoyl-sn-glycero-3-phosphocholine (DHPC) and 1,2-dimyristoyl-sn-glycero-3-phosphocholine (DMPC) (both from Avanti Polar Lipids, >99%) in a 1:3 ratios (q = 3), lyophilized, and then reconstituted in pD 7 buffer with 100 ± 25 mM sodium phosphate and 30 mM sodium chloride (Na_3PO_4, Sigma-Aldrich, 96%; NaCl, Fisher Scientific, ACS grade; DCl and D_2O, Cambridge Isotope Laboratories, 99.5% and 99.8% respectively). For bicelle doping, we replaced 10% mole fraction of DMPC with either 1,2-dimyristoyl-sn-glycero-3-phosphoethanolamine (DMPE), 1,2-dimyristoyl-sn-glycero-3-phospho-

(1'-rac-glycerol) (DMPG), or 1,2-dimyristoyl-sn-glycero-3-phospho-L-serine (DMPS) (all from Avanti Polar Lipids, >99%). Bicelles were prepared by thermal cycling three times in batches and kept refrigerated for up to two weeks until their measurement time. The peptides, [Leu^5]-enkephalin (Lenk) and [Met^5]-enkephalin (Menk) (both from Anaspec, >95%) were exchanged three times with D_2O/DCl to remove residual trifluoroacetic acid and reconstituted in the pD 7 phosphate buffer. When the instrument was ready, the bicelles solution was split into two aliquots. One aliquot was mixed with the peptide, while the second aliquot was diluted with D_2O to achieve the same lipid concentration of 295-300 g/L, a peptide concentration of 30 mM in the peptide aliquot, and a total target volume of 42 µL of pD 7 buffer (without accounting for the volume introduced by the bicelles or peptides). The use of two aliquots allowed for accurate background subtraction in the FTIR and pump-probe measurements. Both aliquots were thermally cycled one more time before use. Finally, we used a 40 mM concentration for peptide in pD 7 buffer, p-cresol in pD 7 phosphate buffer, DMSO (Alfa Aesar, HPLC grade), hexanes (Fisher Scientific, ACS grade) and p-cresol ion in pD 11 phosphate buffer. For simplicity, in the following text and supplementary material we refer to the lipids (DMPC, DMPE, DMPG, and DMPS) by their headgroups (PC, PE, PG, and PS). For bicelles, we refer to those with dopants by the doping headgroups and denote the undoped bicelles as PC.

II.B. Linear FTIR

We immediately acquired FTIR spectra after preparing the sample and background aliquots. All FTIR spectra were acquired on a Jasco 4700 FTIR purged with N_2 gas. FTIR spectra were taken in matched Harrick cells with a 25-µm Teflon spacer and CaF_2 windows for all samples. The FTIR data was processed by first subtracting a water vapor absorption reference spectrum, and then by performing background subtraction using an asymmetric least squares algorithm[57] in a 100 cm^{-1} range surrounding tyrosine ring mode. This directly yielded an undistorted IR line shape and background free baseline for the tyrosine ring mode.

Temperature dependent studies were performed using the same FTIR spectrometer and with a water-cooled Harrick temperature controlled demountable cell that accepted the same CaF_2 window/spacer combination as the normal FTIR measurements. The heating elements,

thermocouple, and temperature controller (CNI16D54-C24) were from Omega. The chiller used to acquire low temperatures was Thermotek T255P. All data was taken in a single batch, starting from a low temperature of 7°C and increasing by 10°C increments up to 77°C. In addition, the sample temperature was equilibrated for an additional 10 minutes after the thermocouple temperature stabilized at the desired set point.

II.C. 2D IR

Pump probe and 2D IR data were acquired immediately after taking the FTIR spectra. We acquired peptide data before acquiring background data. The data was collected using a pump-probe geometry 2D IR setup (Figure S1). The probe incident on the sample was polarized at 45° with respect to the table and picked up with an analyzer set to s-polarization for transmission and to p-polarization for reflection. Detection of probe intensity in both polarizations on a 2x32 MCT array (Infrared Systems Development Corporation) allowed for simultaneous acquisition of <ZZZZ> and <YYZZ> 2D IR spectra. The 2D IR data shown in this work is primarily of the <ZZZZ> polarization and the other polarization was used to determine the vibrational lifetime (Figure S7 and Figure S8) and the rotational anisotropy (Figure S9). The pump pulses were s-polarized and the double-pulse delay was generated with an AOM-based pulse shaper.[58] The pump-probe delay, T, was scanned up to 10 ps using a computer-controlled translation stage for the 2D IR spectra. Shot-to-shot probe pulse fluctuations were removed using our recently developed multi-channel "smart referencing" algorithm,[43] where the reference beam was detected on an unmatched home-built spectrograph and a 1x64 MCT array (Infrared Systems Development Corporation). After the referencing algorithm, the data was Fourier-transformed along the pump delay, τ, and used without any further processing or interpolation. The probe frequency axis is denoted as ω_t.

II.D. Computational

Anharmonic DFT Calculations were performed using the Gaussian 03 package[59] with functional B3LYP and basis 6-31g+ (d,p) with integration grid set to ultrafine and convergence criteria to tight on p-cresol-OD. Response function fitting was performed using the global optimization toolbox in MATLAB 2015a, which was also used for all other numerical calculations.

III. RESULTS

III.A. FTIR:

We first performed FTIR measurements for both Lenk and Menk in the various membrane conditions and in pD 7 buffer, and for p-cresol in pD 7 buffer (Figure 2). Figure S2 shows p-cresol in pD 11 buffer and DMSO. p-Cresol exhibits an approximately 2 cm^{-1} redshift compared to the peptides. The ring mode in the peptides does not show a significant solvatochromatic shift, which is consistent with other work on this ring mode.[29,30,34] The most prominent feature is an asymmetric line shape, with a longer tail on the red-side of the spectrum. This asymmetry is present in all spectra acquired of the ring mode and has been observed in other aromatic vibrational probes.[60] We believe that this asymmetry is most likely caused by vibrational hot-bands: thermally-populated low frequency modes that are anharmonically coupled to the observed ring mode.

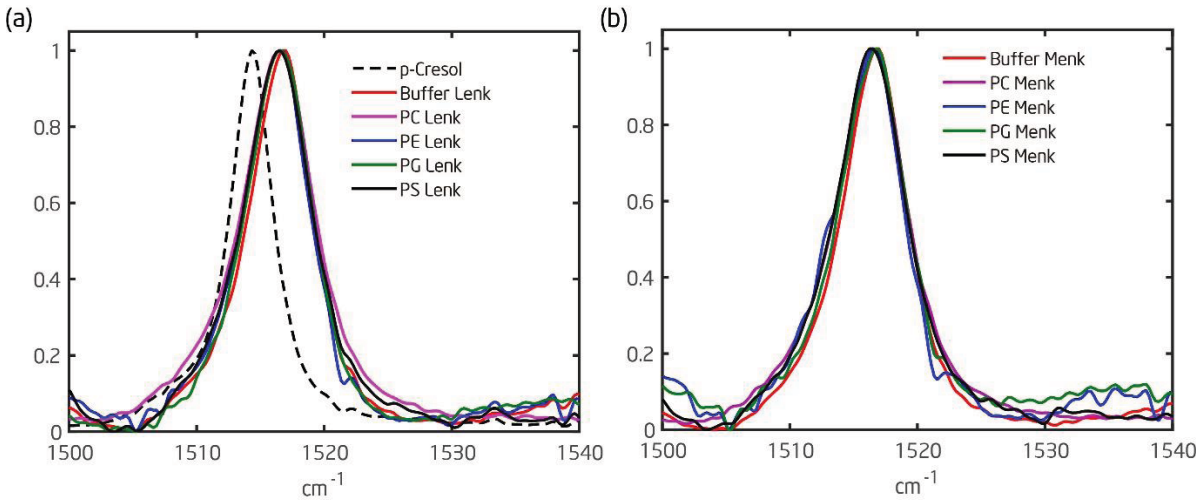

Figure 2. Normalized FTIR data comparing (a) Lenk and (b) Menk in different bicelle conditions. The spectrum of p-cresol in pD 7 buffer is show in (a) in a dashed line. The concentration of the peptides was 30 mM in bicelles and 40 mM in buffer. The concentration of p-cresol was also 40 mM. Unnormalized spectra are available in the supplementary material (Figure S3 to Figure S5).

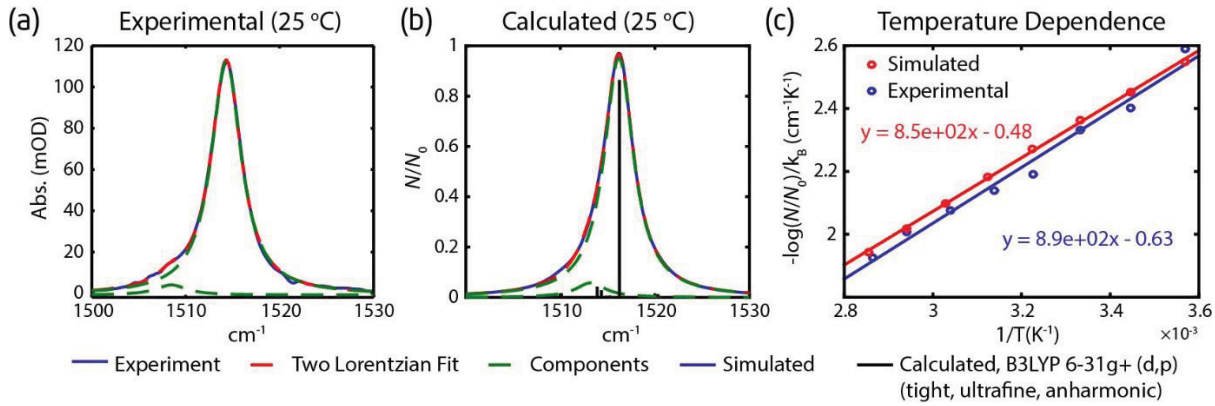

Figure 3. Temperature-dependent FTIR spectra of the tyrosine-ring mode of p-cresol in pure D_2O. (a) Experimental data at 25 °C (blue) with the fit (red dashed) to two Lorentzian components (green dashed). (b) Calculated spectra at 25 °C. The fit to two Lorentzian components in (a) is reproduced with simulated data in red dash. The simulated spectrum that includes multiple hot bands based on anharmonic DFT calculations is shown in blue solid. The underlying cold and hot component spectra are shown in green dashed with the populations shown as black sticks. (c) Temperature dependence of relative hot band population. Experimental data (blue circle). Linear fitting of the experimental data to a single Boltzmann factor (blue line). Simulated data (red circle) based on the calculated spectra that include multiple hot bands based on anharmonic DFT calculations. Linear fitting to the simulated data is shown in red.

To test this hypothesis, we performed temperature dependent FTIR on p-cresol in pure D_2O and anharmonic DFT calculations (B3LYP 6-31g+ (d,p)) for p-cresol-OD in vacuo using Gaussian 03[59] (results summarized in Figure S6 and Table S1). The overall results are shown in Figure 3. After subtracting the temperature-dependent solvent background for the FTIR, we fit the asymmetric line shape to the sum of two Lorentzians of equal width, as shown in Figure 3 (a). The amplitudes of these two Lorentzians represents the relative populations of "cold" and red-shifted "hot" p-cresol molecules, where the IR transition for the "hot" molecules is from a vibrationally excited "hot" mode to a combination mode between the "hot" and c.a. 1515 cm^{-1} "cold" transition. When these two modes are anharmonically coupled, the transition to the combination band exhibits an anharmonic red shift of several cm^{-1}, which allows us to distinguish between these two populations in the FTIR. We fit the relative population of the hot-band to the Boltzmann factor, $I_{Hot}/I_{Total} = e^{-\omega/k_B T}$, as a function of inverse temperature $-k_B \log(I_{Hot}/I_{Total}) = \omega/T$, where T is the temperature used in the FTIR measurements, as

shown in Figure 3 (c). The fit suggests that the frequency ω of the coupled low frequency mode is at approximately 880 cm^{-1}.

The linear fit also gives a large intercept, which is unphysical according to our model. This intercept suggests that there may be contributions from multiple low-frequency modes. When repeating the same fitting procedure with temperature-dependent spectra generated from the anharmonic DFT calculations, we found a similar slope and intercept (Figure 3 (c)). These temperature-dependent spectra were generated by adding together a "cold" Lorentzian peak at 1516.3 cm^{-1} with several "hot" Lorentzian peaks, shifted away from 1516.3 cm^{-1} by their anharmonic frequency shift, for each coupled mode that had an anharmonic frequency shift more negative than -1.5 cm^{-1} (9 modes total, see Figure S6 and Table S2 for anharmonic shifts). The intensities of these peaks were weighted by the Boltzmann factor $\exp(-\omega_i/k_BT)$, where ω_i is the i^{th} coupled mode's anharmonic vibrational frequency. The weight of the fundamental peak was taken to be one minus the sum of all the coupled peak weights such that the sum of all weights was one. We took the half width at half maximum for all peaks to be 1.8 cm^{-1}. An example of such a calculated spectrum is shown in (Figure 3 (b)), where the height of the black bars represents the weight used for each peak.

The anharmonic shifts from the DFT calculations suggest that several coupled ring modes significantly contribute to the shoulder in the FTIR spectrum. Because of the Boltzmann weighting, the lowest frequency modes contribute the highest amplitude. The strongest contributing modes have anharmonic frequencies of 648 cm^{-1}, 730 cm^{-1}, 845 cm^{-1} (see Table S1 for a list of harmonic and anharmonic frequencies). These FTIR and DFT results indicate that the tyrosine ring has a system of several anharmonically coupled ring modes.

III.B. 2D IR:

We performed 2D IR measurements to gain insight into the sensitivity of the tyrosine ring mode to its local environment. In Figure 4 (a), we show 2D IR data of Lenk in PC bicelles as a representation for all measurements performed (see Figure S10 through Figure S20 for remaining data). At waiting time T < 0.5 ps, all the 2D IR spectra exhibit typical spectral signatures of a single-oscillator including a positive peak for excited state emission and ground

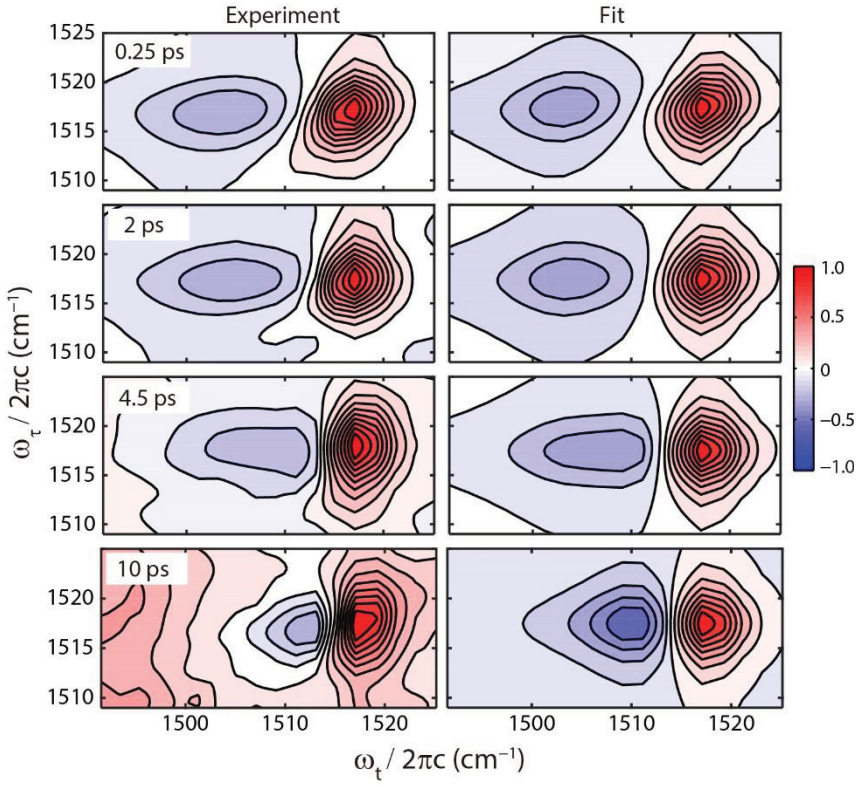

Figure 4. 2D IR spectra of Lenk in PC bicelles at four waiting times, T, as indicated in the panels: (left) experimental data; (right) response function fit based on the IVR model shown in Figure 6.

state bleach and a negative peak for excited state absorption. For all spectra, these peaks are homogenously broadened and have varying degrees of inhomogeneous broadening. At a longer waiting time, there is a distinct blue-shift along ω_t in the frequency of the excited state absorption peak. This shift has been previously attributed to intramolecular vibrational energy redistribution (IVR): ultrafast energy relaxation from the $v = 1$ state to an anharmonically coupled dark state ($1'$).[60-65] The newly shifted peak, which is also observable in the pump-probe spectra, represents the probe excitation from a dark state to a combination band between the dark and bright states. Therefore, the shift is the manifestation of the decay of the bright $v = 1 \rightarrow 2$ transition and the growth of the $v = 1 \rightarrow 1 + 1'$ transition.

One popular procedure that is used to extract the dynamic observable of interest, the FFCF, is the center-line-slope (CLS) method.[66,67] Briefly, this method takes slices of the $v = 0 \rightarrow 1$ transition along ω_t as a function of ω_τ, extracts the maximum point for each slice, and fits a

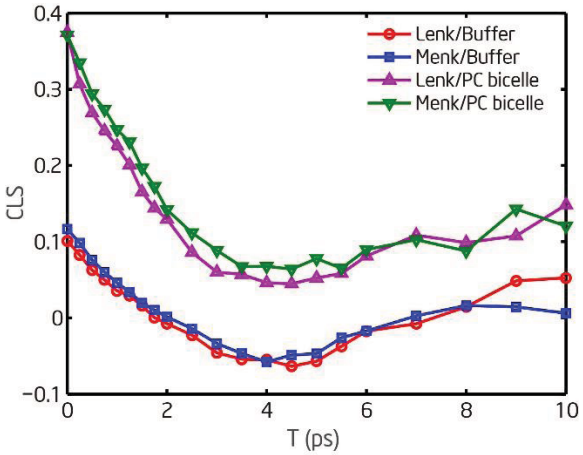

Figure 5. CLS data for Lenk and Menk in pD 7 buffer and PC bicelles.

line through the points (see Figure 9 below as an example). The slope ($d\omega_t/d\omega_\tau$) as a function of T has been shown to be proportional to the FFCF within certain limits.[66] The advantage of this method is that the FFCF estimation is more robust compared to a full response function fit because the number of free fitting parameters is smaller. Unfortunately, the CLS method is highly susceptible to systematic error that can be introduced by complex line shapes or experimental noise. As an example, Figure 5 shows a representative sample of CLS plots as a function of waiting-time, which all exhibit a prominent dip at around 4-5 ps (see Figure S23 for all plots). Therefore, we were unable to directly use the CLS method to extract the FFCF.

III.C. Modeling the 2D IR spectra with an IVR model

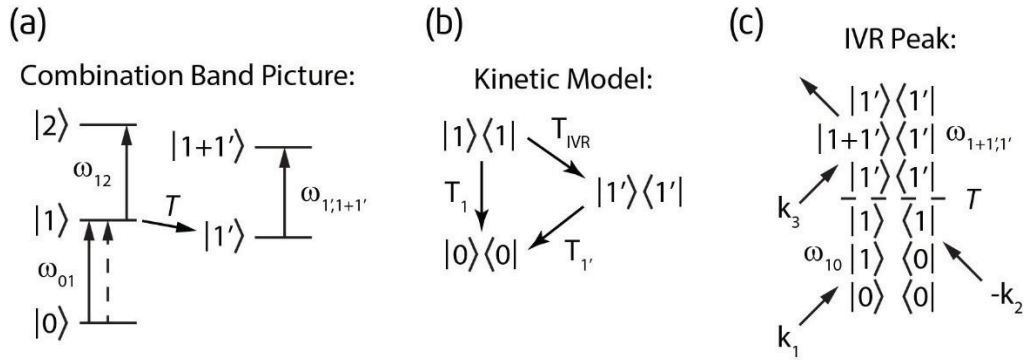

Figure 6. Summary of the IVR model. (a) The combination band picture. (b) The kinetic model describing population relaxation. (c) The Feynman diagram that corresponds to the non-rephasing IVR peak.

To gain more insight into the dynamics and to attempt to extract the FFCF, we performed a global 3rd order response function fit that includes a kinetic model for IVR during the population evolution period. We summarize diagrammatically the key features in Figure 6. The model consists of a 5-level system that includes the $v = 0$, $v = 1$, and $v = 2$ tyrosine ring mode states, as shown in Figure 6 (a). Irreversible energy transfer is allowed between the $v = 1$ and a dark state, $v = 1'$, which can be further excited to the combination band $v = 1 + 1'$. All population relaxation dynamics are modeled using the kinetic model shown in Figure 6 (b), where T_1 and $T_1{}'$ are the vibrational population relaxation times of the 1 and $1'$ states, respectively, and T_{IVR} is the IVR time. The model does not include reorientation dynamics because the peptide's rotational correlation function decays much more slowly compared to the vibrational lifetime of the ring mode (see Figure S7-Figure S9 for lifetime and anisotropy data). Spectral diffusion is included in the model using the second-order cumulant expansion and with the model FFCF:[29]

$$C(t) = \gamma_0 + {\Delta_1}^2 e^{-\frac{t}{\tau_1}} + {\Delta_2}^2 \quad (1)$$

where Δ_1 is the magnitude of frequency fluctuations in the spectral diffusion, τ_1 is the timescale of spectra diffusion, $\gamma_0 = 2\delta(t)/T_2^*$ is the pure dephasing contribution, and Δ_2 is the static inhomogeneity.

To calculate the 2D IR spectrum, we first calculate all the rephasing and non-rephasing response functions as a function of τ, t, T. We assumed fully correlated $v = 0 \rightarrow 1$ and $v = 1 \rightarrow 2$ transitions, for which the analytical form of these response functions has been tabulated elsewhere.[68,69] Figure 6 (c) shows one of the non-rephasing Feynman diagrams that involve energy transfer during T. The sum of these pathways is then Fourier-transformed (using a discrete Fourier-transform) directly to the calibrated experimental ω_τ and ω_t frequencies. We use a nonlinear least-squares fitting procedure that fits the 3rd frequency-domain response functions directly to the 2D IR data (see the supplementary material section S6 for more detail and Figure S10-Figure S20 for results).

The fit reproduces the 2D IR, pump-probe spectra, and FTIR spectra quite well, but the fitted parameters are not robust due to overparameterization. When we repeated the CLS

method on the simulated 2D spectra from fitting, we found that the resulting waiting-time dependence cannot reproduce the prominent dip. Using this procedure, we also found that the extracted FFCF correctly reproduces the input parameters (up to a scaling factor). Therefore, the prominent dip in the CLS does not directly come from the energy transfer during the population period.

Upon closer inspection, the 2D data shows an unusual line shape distortion that occurs around T = 4.5 ps for all spectra acquired except for p-cresol in DMSO where this distortion occurs at T = 2 ps and for p-cresol in pD 7 buffer where the distortion is difficult to resolve. The apparent result of this distortion is the red shifting of the new IVR peak along the pump axis, ω_τ, as a function of T (Figure S22). The feature is also present in the p-cresol anion (see Figure 11 below), where the ring mode is red-shifted from the p-cresol neutral molecule by 14 cm^{-1} in the linear IR (see Figure S2). Therefore, the distortion is unlikely to be caused by noise (either random or static) or instrumental error because of its repeatability.

We consider three models that may explain this line shape distortion: (1) population exchange with hot states, (2) local environment dependent IVR rate, and (3) fast reversible coherence transfer between the bright and dark states. The first model does not introduce this line shape distortion but does reproduce several subtle features of the 2D IR spectra. The second model recovers the effect of the line shape distortion but requires a static inhomogeneity that is not present in all samples. The third model also recovers the line shape distortion but introduces additional distortions that are not immediately apparent in the data. In Section III D, we discuss each model in detail and show their effects on the CLS.

III.D. Modeling the 2D IR spectra with three advanced models

III.D.1. Population exchange with hot states

The first model, population exchange with hot states, is motivated by the fact that the hot-band shoulder present in the FTIR should also be present in the 2D IR spectra. Assuming that the hot and cold bands have the same transition dipole and dephasing dynamics, the peak intensity ratio in both the 2D IR and FTIR will be approximately the same and depend on relative populations determined by the Boltzmann factor. Therefore, we expect, from the FTIR fit, a ~5%

contribution at room temperature. Furthermore, we expect that the hot population will exchange with the cold population on a 2D IR accessible timescale,[70,71] which will lead to cross peaks that will interfere with the overtone and IVR combination peaks.

We implement this model by adding the kinetic model described in Figure 7 to the response function fit in the previous section. The resulting kinetic model for the population evolution period, T, includes the irreversible IVR decay detailed in Figure 6 (b) plus the reversible exchange to corresponding hot states for all three cold populations. The ratio of the forward (cold to hot, k_f) and backward (hot to cold, k_b) exchange rate is determined by the steady state population ratio between the hot and cold states, which is equal to the Boltzmann factor. The forward exchange rate is left as a free parameter. Finally, we assume that the energy fluctuations in all populations generated remain fully-correlated during any population exchange.

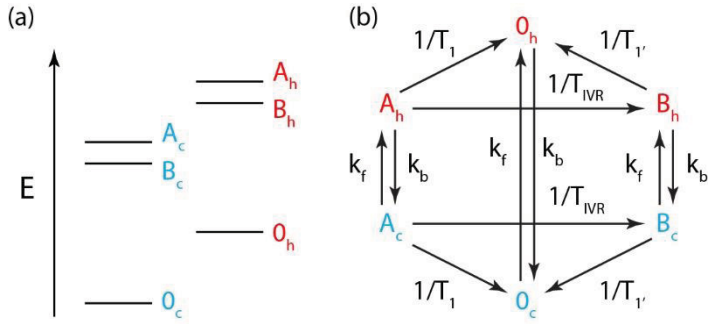

Figure 7. (a) Level scheme diagram showing the states involved in the hot-states exchange model. State A represents the first excited state of the tyrosine ring mode. State B represents the dark state. State 0 represents the ground state. The subscript h (c) and red (blue) color denote the hot (cold) species. (b) Kinetic scheme for the hot-states exchange model.

Given the assumptions made, the 2D IR spectra are straightforward to calculate. First, in our model the pump can be thought of as generating a non-equilibrium population of transition dipole-allowed states. The kinetic model then describes how each non-equilibrium population decays back to equilibrium as a function of T. Therefore, we implement the kinetic model as a T-dependent transfer matrix, $\boldsymbol{M}(T)$, that maps pump-generated populations to populations that the probe acts on. The pump (probe) is represented as a matrix where each row (column) represents a discretized function τ (t) that is summed over, for a given population, the half of

the Feynman diagrams before (after) T-evolution. Finally, because we assume all oscillators have fully correlated FFCFs, we multiply the response function by the exponential of the line shape function. The full computational detail of this method and the population dynamics of hot and cold species are given in the section S10 of the supplementary material and Figure S25.

The hot-states population exchange model generates several new subtle features in the simulated 2D IR spectrum (Figure 8). First, the $v = 0 \rightarrow 1$ transition now exhibits a red-side shoulder which is due to the hot band peak. Second, this tail persists at long T, slightly altering the peak shape. Finally, due to population exchange and the cancelation with the IVR peak, both $v = 0 \rightarrow 1$ and $v = 1 \rightarrow 2$ peaks have a slight additional broadening along ω_τ. We note that this model cannot reproduce the line shape distortion because the hot-state populations are too small.

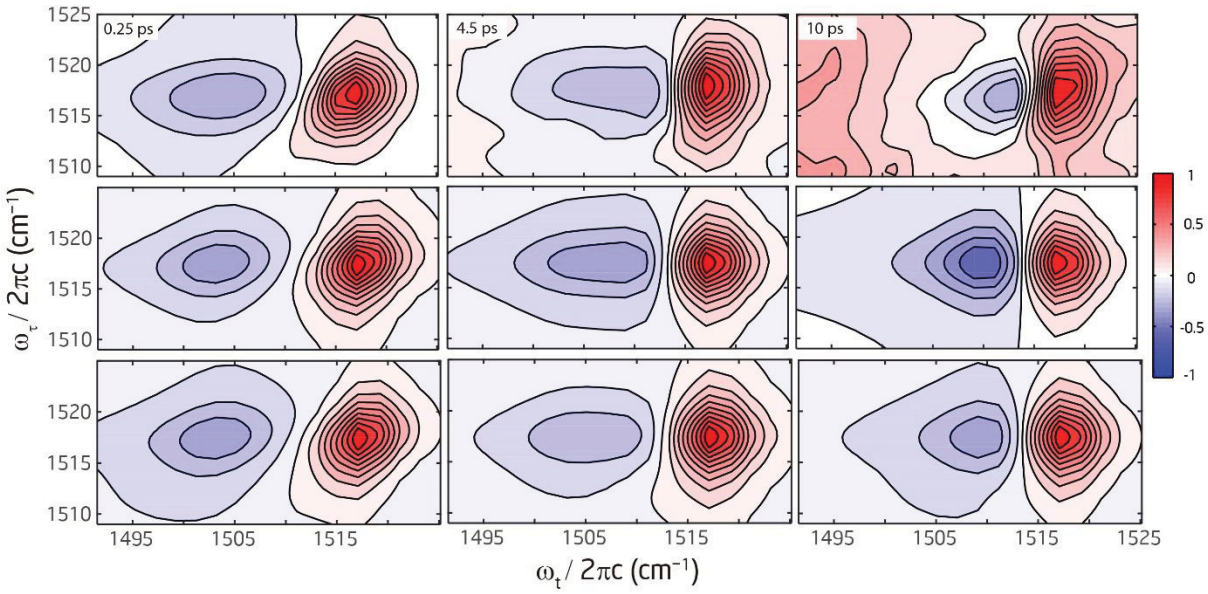

Figure 8. Comparison of the hot-state exchange model (3rd row), with the response function fit (2nd row) and the experimental data (1st row) for Lenk in PC bicelles. The 3rd row takes parameters from the fit (2nd row) and adds a set of hot band peaks that correspond to a hot mode at 650 cm^{-1} at 300 K that induces an anharmonic shift of 5 cm^{-1} and hot-to-cold exchange rate constant of 5 ps^{-1}.

III.D.2. Local environment dependent IVR model

The local environment dependent IVR model involves the reconstruction of the line shape distortion by the interference of two or more spectrally separated populations with different IVR rates, $1/T_{\mathrm{IVR}}$. In this model, the relaxation dynamics depend on the local environment and the transition frequency. To reconstruct the line shape distortion, the shifting of the $v = 1 \rightarrow 2$ peak into the IVR peak happens much faster for the lower-frequency population than the higher-frequency population. Note that the apparent shifting of the $v = 1 \rightarrow 2$ peak happens at the vibrational relaxation rate (the sum of the rates of all possible relaxation pathways) and not at $1/T_{\mathrm{IVR}}$ directly, which is a direct consequence of the kinetic model in Figure 6 (b). In the kinetic model, the $v = 1 \rightarrow 2$ peak decays and IVR peak grows in at the same rate of $1/T_1 + 1/T_{\mathrm{IVR}}$.

To show that vibrational relaxation is local environment dependent in our system, we turn to p-cresol in DMSO and pD 7 buffer. The ring mode's peak frequency in DMSO is 2 cm^{-1} blue-shifted from that in pD 7 buffer (Figure S2). Its vibrational lifetime is 1.6x shorter in DMSO than in pD 7 buffer (see the decay time constant of $v = 1 \rightarrow 2$ peak, τ_1, in Table S3 and Figure S8). Interestingly, the response function fit (Table S4 and Figure S10 and Figure S11) suggests that the 1.6x shorter vibrational lifetime of p-cresol in DMSO is caused by a 3.8x faster IVR time constant (T_{IVR}) and not by other relaxation channels (T_1). With this evidence, we believe that such a model is possible for our system, and we provide further comment on possible physical origins in the discussion.

We construct this model by approximating local environment inhomogeneity with two populations with their $v = 0 \rightarrow 1$ frequency separated by 2.5 cm^{-1}. The framework for this model is the same as the population exchange response-function model in the previous section III.C, but with two key differences: first, the ratio of the two populations is assumed to be 1:1 to maintain the symmetry of the peak in the linear IR spectra and to minimize the number of parameters, and therefore the forward and backward exchange rates between them are the same if they undergo chemical exchange; and second, the lower-frequency population has a 6 times faster IVR rate as compared to the higher-frequency population. This much faster IVR rate was required to reproduce the line shape distortion. The results of the simulated 2D IR spectra

are summarized in Figure 9. The line shape distortion is well reproduced in the case of no exchange (bottom row) between the two populations (i.e. static inhomogeneity), which is typical for peptides in bicelles.

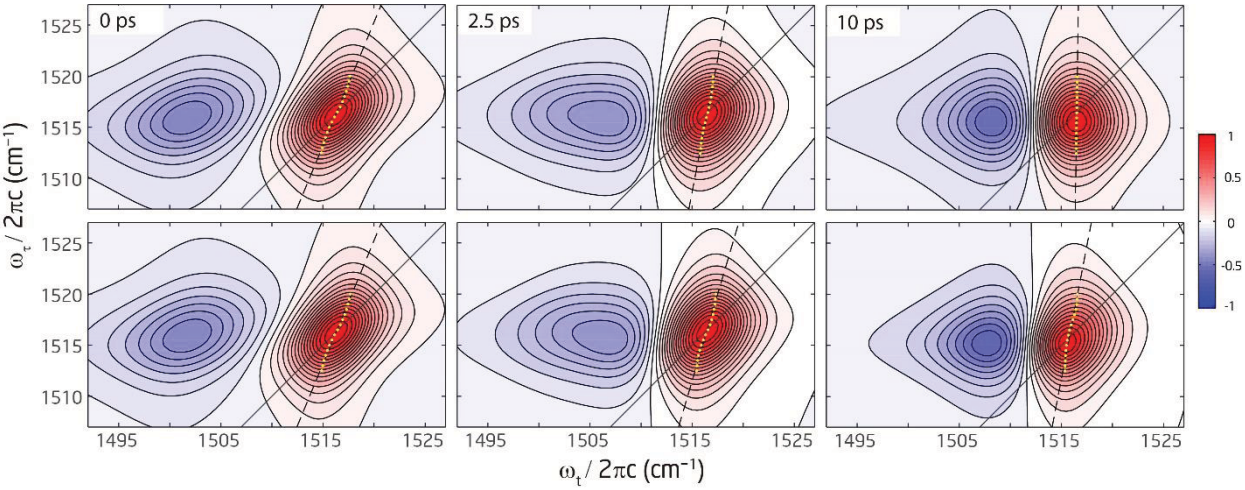

Figure 9. Simulated 2D IR spectra based on the local environment dependent IVR model with chemical exchange (5 ps^{-1}, top) and without chemical exchange (bottom). The ratio between the IVR rate of the low frequency peak and that of the high frequency peak is 6:1. Peak maxima for slices along ω_t are shown as yellow dots and the center line is shown as a dashed black line. The simulated CLS plots are shown in Figure 13 (a) for a variety of exchange and IVR energy transfer rates.

Including population exchange allows for this model to mimic systems dominated by spectral diffusion without much static inhomogeneity (Figure 9, top row), including the peptide in pD 7 buffer and the p-cresol anion in pD 11 buffer. One trend we observed is that the addition of this exchange process generates cross peaks that can somewhat diminish the line shape distortion. The higher the exchange rate, the faster the IVR rate on the lower-frequency mode is required to reproduce the line shape distortion. We note that a faster energy transfer rate should lead to faster dephasing and therefore a broader peak, but we do not consider the effect of IVR on dephasing in this model. To summarize, the local environment dependent IVR model visually reproduces the line shape distortion best when static inhomogeneity is present. The effects on the CLS are discussed in IV. Discussion.

III.D.3. Fast reversible coherence transfer between bright and dark states

So far, we have only considered the effect of energy transfer during the population evolution period. It is also possible to generate a similar line shape distortion by including coherence transfer to the dark state. In this case, the line shape distortion is caused by the interference of inter-state coherences generated between the bright and dark states. The advantage of such a model is that it does not require local environment inhomogeneity with very different relaxation rates.

To include coherence transfer, we propagate the density matrix directly using a phenomenological set of rate equations based on Redfield theory following a procedure described by Khali et al.,[72] but with the exclusion of rotational dynamics. The procedure consists of two main parts: (1) propagation of the density matrix via the master equation and (2) operating on the density matrix with the transition dipole operator. The density matrix is propagated in Liouville space via the master equation:

$$\dot{\rho} = (\Gamma + i\omega)\rho \tag{2}$$

where ρ is the density matrix in Liouville space, Γ is the tetradic Redfield tensor in matrix form, and ω is a diagonal matrix of transition frequencies. In the Markovian limit, the Redfield tensor is time-independent and can be thought of as a kinetic model between different diagonal elements and between different off-diagonal elements of the density matrix.[72] In this limit, the solution to the time propagator can be written directly, assuming $t \geq 0$:

$$\mathcal{G}(t) = e^{(\Gamma + i\omega)t} \tag{3}$$

The 2D IR spectrum is calculated in the time domain via step (2) by iteratively operating with the transition dipole superoperator, $\mathcal{V}_{ij,mn} = V_{jm}\delta_{kn} - V_{kn}\delta_{jm}$,[73] and time propagator $\mathcal{G}(t)$. The transition dipole operator, V, is a matrix of the magnitudes of transition dipole moments for all allowed and forbidden transitions (if the transition is forbidden, the matrix element is zero). The response function is calculated by:

$$R(t, T, \tau) \propto \langle\langle V(\mathcal{G}(t)\mathcal{V}\mathcal{G}(T)\mathcal{V}\mathcal{G}(\tau)\mathcal{V})\rho_0\rangle\rangle \tag{4}$$

where $\langle\langle \dots \rangle\rangle$ represents the trace over the density matrix and where ρ_0 is a column vector representing the equilibrium density matrix. For our model, ρ_0 has the element corresponding to the ground state population set to 1 while all other elements set to zero. The final V represents

the transition dipole operator acting from the left. As written, Eq. 4 represents all possible interactions with the light field, integrated over all directions. To extract the components that contribute to the 2D IR signal, one must keep track of phase-matching in the transition dipole operator. To do this, we partition $\mathcal{V}$ into $\mathcal{V}^+$ and $\mathcal{V}^-$, which correspond to interactions with fields of wavevector $+k$ and $-k$, respectively. The rephasing and non-rephasing response functions are then calculated separately:

$$R_R(t,T,\tau) \propto \langle\langle V^-(\mathcal{G}(t)\mathcal{V}^+\mathcal{G}(T)\mathcal{V}^+\mathcal{G}(\tau)\mathcal{V}^-)\rho_0\rangle\rangle \tag{5}$$

$$R_{NR}(t,T,\tau) \propto \langle\langle V^-(\mathcal{G}(t)\mathcal{V}^+\mathcal{G}(T)\mathcal{V}^-\mathcal{G}(\tau)\mathcal{V}^+)\rho_0\rangle\rangle \tag{6}$$

Finally, the two response functions are Fourier-transformed and added in the usual way to get the absorptive spectra. This greatly simplified form of the calculation is possible because we do not consider rotational dynamics. As a result, we do not need to keep track of any coordinate frame for the transition dipole operators so that all transitions can be considered simultaneously.

Using the diagram notation introduced by Khali et al.,[72] Figure 10 (a) summarizes the key parameters used in the model. The dark state |1'> is assumed to have a lower fundamental frequency than the bright state |1>. Any transition directly involving the dark state will have matrix element value of zero for the transition dipole operator. Therefore, any coherence involving the dark state directly will not be observable. This means that the coherence transfer needs to be reversible to be observable, otherwise it will not be distinguishable from dephasing. For simplicity and to see the effect of coherence transfer clearly, this model includes only homogeneous broadening, but not spectral diffusion nor static inhomogeneity.

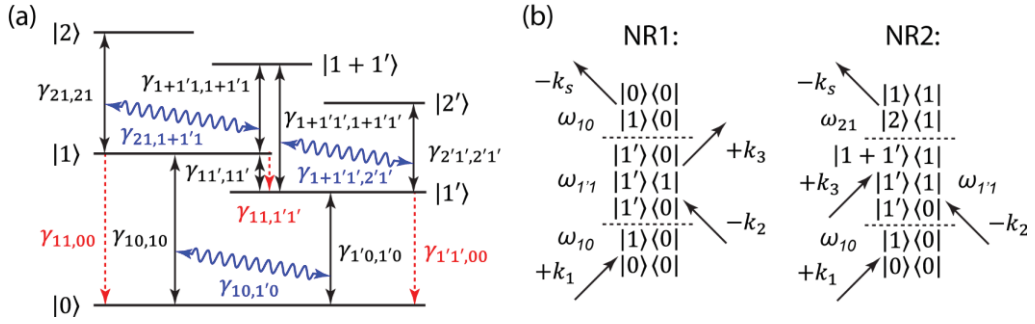

Figure 10. (a) A level scheme diagram showing all the energy transfer processes in the simulation. Black up-and-down arrows represent dephasing of a coherence. Blue diagonal wavy arrows represent coherence transfer. Red dashed down arrows represent population transfer and relaxation. (b) Feynman diagrams showing the two allowed coherence transfer pathways.

When coherence transfer to the dark state is included, several new features appear in both the 1D IR and 2D IR spectra. For the 1D IR spectra two features appear: first, the apparent transition frequency of the mode redshifts because of motional narrowing; second, a prominent dip appears at the frequency of the dark state. These two effects can be directly explained in the time-domain. At short t, the coherent oscillator |1><0| transfers to the dark state |1'><0|, which oscillates at a lower frequency. Therefore, when the coherence is transferred back, it is done so with a phase lag. The interference between the unlagged and phase lagged oscillators causes the line shape distortion. Intuitively, the presence of the dark state slows down the bright oscillator (this causes the red-shift) and phase-lag leads to destructive interference between the oscillators, which causes the dip.

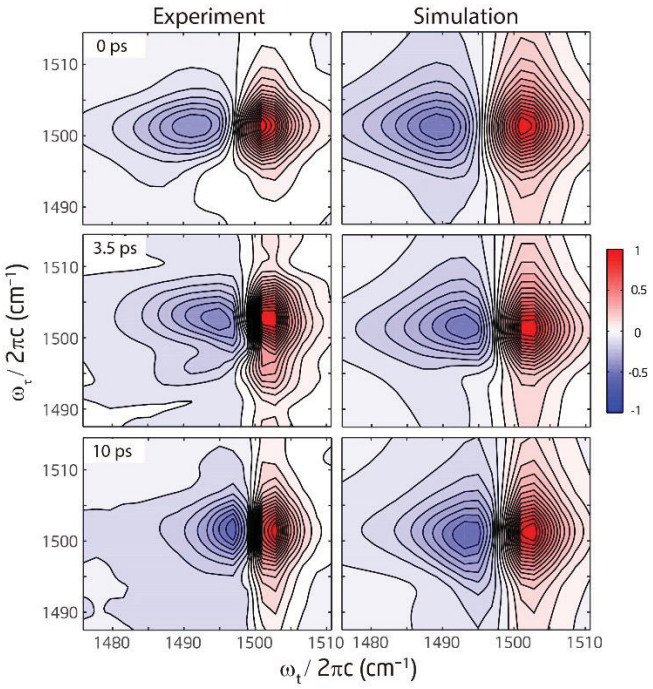

Figure 11. Experimental 2D IR spectra of the p-cresol anion in pD 11 buffer (left). Simulated 2D IR spectra with the coherence transfer model (right).

For the 2D IR spectrum, an additional peak is introduced that helps visually reproduce the line shape distortion present in all experimental data and does so most clearly in the p-cresol anion (Figure 11). This new feature can be understood by careful analysis of the different possible Liouville pathways, which reveals that only two pathways contribute to T-dependent

dynamics as shown in Figure 10 (b). Both pathways generate an interstate coherence between the bright and dark states. These pathways are closely related to on-diagonal cross-peaks which are generated in the case of two coupled oscillators by non-rephasing pathways.[68,69,74] The frequency domain equivalent is analogous to a non-rephasing 2D Lorentzian that cycles through its phase at the frequency difference between the bright and dark state. The line shape distortion in the experimental data can be reproduced when the dephasing of the interstate coherence is long enough to include only a single oscillation.

In addition, several new distortions that are not present in the experimental data are also introduced by the model. First, a red-side dip appears in the simulated 1D spectrum, which is also present in the simulated 2D spectra as a sudden drop in peak intensity along ω_τ (not shown), whereas our experimental data shows a shoulder. The addition of hot-bands to the model is not sufficient to recover the shoulder in this case. Second, the nodal line slope[75,76] in the simulated 2D IR spectra is negative at short T, whereas the experimental data has a positive slope. It is possible that the addition of spectral diffusion may overcome this distortion. Given these distortions, we believe that, although coherence transfer may be present, it is not a significant contributor to the experimentally observed line shape distortion.

IV. DISCUSSION

IV.A. Many coupled ring modes

The presence of multiple hot-bands in the FTIR spectra suggest that the tyrosine side-chain potential energy surface is composed of several mechanically coupled ring modes, which is also supported by DFT calculation (Figure S6, Table S1, and Table S2). This network of coupled ring modes, and their combination bands, likely provide efficient relaxation channels for vibrational energy. The presence of these relaxation channels is evidenced in the 2D IR spectra as a T-dependent anharmonicity, where the $v = 1$ vibrationally excited state population relaxes to a dark state that is likely composed of a combination of lower energy ring modes. The fact that this feature is present in both p-cresol and in Lenk and Menk in a variety of environments strongly suggest that this feature is directly related to the ring.

For the initial energy relaxation to satisfy detailed balance, the ratio of the backward and forward rates must be proportional to the Boltzmann factor. Our experimental data shows an irreversible energy transfer where the $v = 1 \rightarrow 2$ peak decays fully as the $v = 1 \rightarrow 1 + 1'$ IVR peak grows in. This irreversibility can either be accomplished by having a dark state energy substantially lower than the bright state, or by having a bath of many coupled dark states. In the first case, the energy difference between the bright and dark state needs to be >> $k_B T$, but the bath is unlikely to readily accept such a large amount of energy, unless it involves a discrete solvent molecular mode.[77-79] Therefore, the first case will likely have a slow relaxation rate.

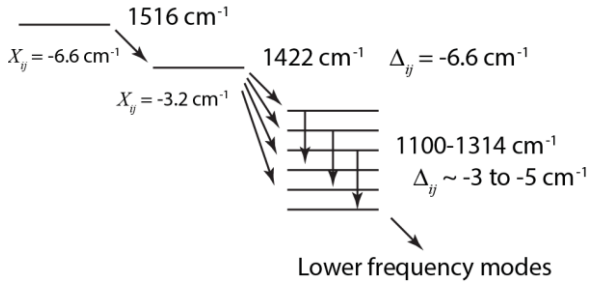

Figure 12. Figure showing the level scheme diagram for p-cresol based on the DFT calculations (Figure S6, Table S1, and Table S2). X_{ij} and Δ_{ij} are anharmonic couplings and anharmonic frequency shifts, respectively.

We believe that the second case is more likely because our DFT calculations indicate that there are many coupled low-frequency modes that involve the ring and their frequency separation from the ring mode is within the available solvent density of states (DOS). Based on the coupling map shown in Figure S6, we propose a dominant relaxation channel in Figure 12. Here, the 1422 cm^{-1} ring C-H wagging mode provides a vibrational energy relaxation pathway from the fundamental 1516 cm^{-1} mode to several ring modes between 1314 and 1100 cm^{-1}. In this picture, each step requires release of <100 cm^{-1} of energy, which is easily facilitated by the solvent at room temperature. The IVR peak then represents a vibrationally hot ring and the "dark state" is instead a thermal reservoir of many modes delocalized over the ring. Because these modes are anharmonically coupled to the fundamental 1516 cm^{-1} mode, the probe absorption is red shifted in a similar way as "hot" p-cresol molecules introduce a red-shifted shoulder in the FTIR. When energy is dissipated away from the coupled ring modes into states that are not

coupled with the fundamental transition (i.e. the solvent or uncoupled solute modes), the IVR peak attains a zero-frequency shift. The IVR peak then destructively interferes with the bleach contribution, thereby causing the slow decay (τ_2 in Table S3) of the remaining peaks at long T. It follows that the decay of the IVR peak represents the vibrational cooling of the ring.

IV.B. Physical origin of local environment dependent IVR model

The faster growth of the p-cresol IVR peak in DMSO, as compared to pD 7 buffer, clearly shows that the IVR rate can be local environment dependent. Because the molecular vibrational state energies and their anharmonicities are unlikely to be changed significantly in weakly interacting solvents, the relaxation rate is likely to be related to the solvent's ability to accept the ring mode's vibrational energy. The solvent can accept vibrational energy either through its internal vibrations or through its low-frequency collective vibrations.[78,80] For the case of internal vibrations, DMSO is more likely to facilitate energy transfer because it has more low-frequency internal vibrations as compared to D_2O.[81,82] Neat DMSO has several vibrations bands[81,82] around 300 cm^{-1} which match the energy difference between the bright mode and the set of coupled modes between 1100-1200 cm^{-1} shown in Figure 12.

For the case of low-frequency vibrations of solvent, intuition says that p-cresol in D_2O should show a faster relaxation because of its higher DOS in the 100 cm^{-1} range.[82] These modes would facilitate the relaxation pathway to the 1400 cm^{-1} mode shown in Figure 12, but the opposite is observed (see the faster decay τ_1 in DMSO in Table S3). One explanation is that the hydrophobic effect limits the available DOS (i.e. when solvent/solute coupling is considered) that can act as energy acceptors. The hydrophobic effect has been previously been implicated in explaining the unusual solvent dependence on bandwidth observed for the tyrosine ring mode.[30] One possible microscopic explanation for this hydrophobic effect is that water forms an ordered cage around the ring (i.e. the Iceberg model),[83] limiting the motions of the water molecules in the solvation shell.[84] We speculate that this limited motion can limit the forces felt by the ring, which would lower the coupling-DOS product needed for relaxation.

Indeed, MD simulations suggest that the first hydration shell around benzene has a significant ordering of the water molecules, with hydrogen bonding to the faces of benzene.[85,86]

Because this hydrogen bond is relatively weak and has an entropic driving force for formation,[87] the librational and translational motions of water at the benzene faces are faster compared to those of bulk water.[88] The equatorial region of benzene, on the other hand, displays a more hydrophobic character and ab initio molecular dynamics simulations suggest slower water dynamics. [88] We believe that similar dynamics exist in our system because the π-H-bond has also been identified in tyrosine.[89]

IV.C. Physical origin of the coherence transfer model

The picture just described makes it difficult to rationalize the coherence transfer model because of the following features. First, coherence transfer requires a dark state that is close in energy. To be able to reproduce the dip in the CLS spectra, the interstate coherence must oscillate with a period of approximately 9 ps. Therefore, the dark state must be redshifted by approximately 3.7 cm^{-1}. However, our DFT calculations do not predict any Fermi-resonances with the 1516 cm^{-1} ring mode. It is possible that the dark state is composed of a combination of three or more modes, making it possible that such a state could exist, although the corresponding higher-order couplings are probably weak. Second, the coupling between the bright and dark state needs to be strong enough to allow for fast reversible coherence transfer. Given the near-degeneracy of the proposed states, this may be possible, although one would also expect some amount of mode and transition dipole mixing. Including a small transition dipole for the dark state in the coherence transfer model does not generate a shoulder that can compensate for the red-side dip predicted by the model (simulation not shown). Third, the coherence transfer process must be sufficiently fast to allow for a significant peak interference. In our model, the coherence transfer process is 1.3x faster than population transfer. Although the fitting by Khalil et al. suggests that coherence transfer can be much faster than population transfer,[72] subsequent work by Baiz et al. shows, from a microscopic model involving force correlation functions, that this is unlikely.[90] Finally, there is a discrepancy between the fact that coherence transfer needs to be reversible, while population transfer needs to appear irreversible. Resolving this discrepancy would require that the interferences generated by coherence transfer involve

different states that are distinct from those giving rise to the IVR peak. Therefore, we think that the coherence transfer model is unlikely.

Finally, we emphasize that in the coherence transfer model, the line shape distortion is caused by the oscillatory interference of the on-diagonal cross-peaks (generated by coherence transfer) with the diagonal peaks. While we do not think the following are present in our system, other processes may generate similar oscillating on-diagonal cross peaks and can potentially lead to a similar line shape distortion in the presence of IVR. For example, if there are two coupled states, such as a Fermi-resonance or dimerization and formation of coupled symmetric and anti-symmetric mode pairs, then the non-rephasing on-diagonal cross-peaks between the two states could lead to the peak distortion involved. In this case, two coupled states would still need to be within approximately 4 cm^{-1} of the 1516 cm^{-1} fundamental in order to match the timing of the distortion. We found that 40 mM p-cresol in hexanes forms a coupled dimer, whose FTIR spectrum shows two peaks (Figure S3) and 2D IR spectra exhibit a line shape evolution (Figure S21): the negative feature is stronger at the lower ω_τ peak at the early waiting time and the relative strength in the higher ω_τ peak increases with intermediate waiting times. Note that this evolution of 2D IR spectra does not closely resemble the single oscillator spectra studied in this work, therefore we do not think that our line shape distortion is caused by dimerization. For the case of Fermi-resonance, the coupled dark state would likely still need to be distinct from the states and processes involving the IVR peak. Because DFT calculations did not predict a Fermi-resonance for the 1516 cm^{-1} mode, we did not explore this possibility further.

IV.D. Model effect on CLS

Finally, we consider how each of these models effect the CLS. In Figure 13, we show how the different models change the CLS by comparing the CLS with the model turned on and off, as described in the figure caption. We did not plot the effect of the hot-states exchange model in this figure because it does not visually change the CLS. In Figure 13 (a), the presence of local environment dependent IVR does perturb the CLS, as evidenced by the deviation of the 6:1 curves (model on) from the 1:1 curves (model off). The line shape distortion introduced by the local environment dependent IVR is only present when the peak is inhomogenously broadened

(i.e. slow exchange between the two populations of hot states). If spectral diffusion dominates (i.e. fast exchange), the line shape distortion and its effect on the CLS is diminished at longer T. This result is intuitive considering that in spectral diffusion the oscillator's frequency becomes uncorrelated: at long T, the correlation between IVR rate and the local environment is lost. We also note that the line shape distortion is stronger when the ratio between the two hot-band populations' IVR rates is larger.

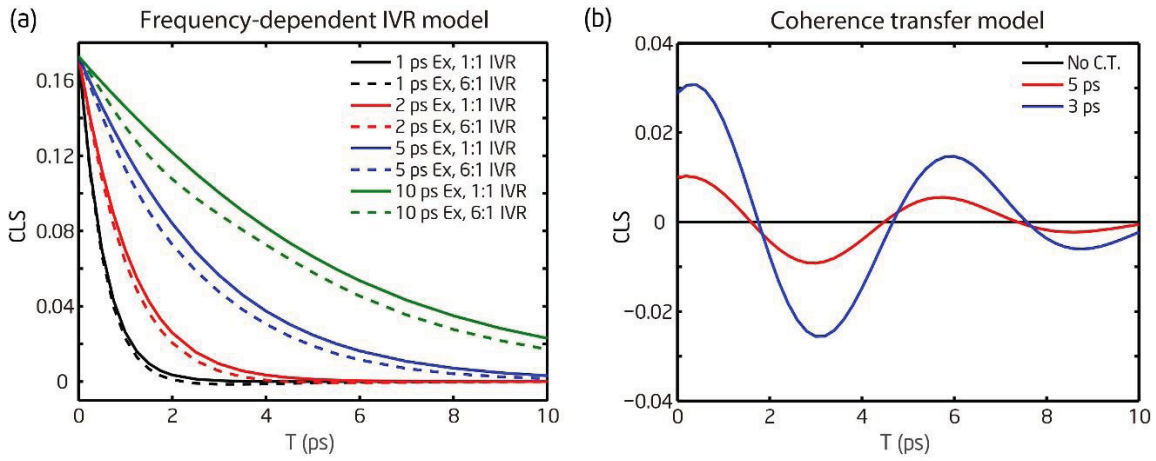

Figure 13. (a) The effects of the local environment dependent IVR model on the CLS. In the legend, the time constant indicates the exchange rate between the lower-frequency and higher-frequency populations and the ratio indicates the ratio between the two populations' IVR rate. The case of fast exchange mimics the situation when the dynamics is dominated by spectral diffusion. The 1:1 IVR curves (solid) represent the model being turned off and the 6:1 IVR curves (dashed) represent the model being turned on. (b) The effect of the coherence transfer model on the CLS. The time constant in the legend represents the coherence transfer rate. Note that the coherence transfer model does not include static inhomogeneity or spectral diffusion, which causes the no coherence transfer case (model off) to be flat (black line).

Although a line shape distortion is present for the local environment dependent IVR model, it only gives rise to a small dip in the CLS vs. T plot for all curves shown, much smaller than the dip feature present in the experimental data. A much stronger change in the CLS is introduced with the coherence transfer model as shown in Figure 13 (b). The presence of an interstate coherence generates an oscillatory feature in the CLS. The oscillation's period corresponds to the oscillation period of the interstate coherence. The amplitude of the oscillation is related to the amplitude of the interstate coherence, which is determined by the

rate of coherence transfer. In addition, the decay of the oscillation is related to the dephasing of the interstate coherence. For the experimental CLS plots in Figure 5 and Figure S23, it is difficult to tell whether there are additional oscillations beyond the prominent dip at around 4-5 ps.

Because the effects of both models on the CLS is diminished at long T, the most reliable fitting parameter is the static inhomogeneity. To see if any trend exists in the CLS data, we fit the data in Figure 5 to a single underdamped oscillation plus an offset:

$$C(t) \propto {\Delta_1}^2 \cdot \cos\left(\frac{2\pi t}{\tau_1}\right) \cdot e^{-\frac{t}{\tau_2}} + {\Delta_2}^2 \tag{7}$$

The results are summarized in Figure 14. The full fitting details and full set of fit parameters are given in Figure S24 and Table S5. The fitting parameter for the static inhomogeneity does show a trend that is consistent with our initial hypothesis: charged and packed lipid surfaces result in less static inhomogeneity, although most of the differences we observe are within experimental error. We previously attributed a larger static inhomogeneity to a larger conformational distribution of the peptide because the peptide conformations exchange on a timescale much slower than picoseconds and also DFT calculations indicate that the tyrosine ring mode frequency is modulated by peptide conformation.[29] Structural simulations with nuclear Overhauser effect (NOE) constraints of Menk in PC and PG lipid bilayers suggest that a surface-bound (in PG) peptide will have less conformational distribution compared to a buried peptide (in PC).[51], consistent with our finding that Menk has a lower static inhomogeneity in PG than in PC.

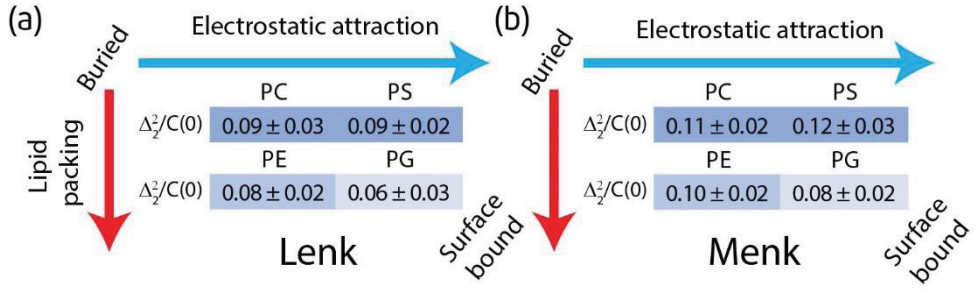

Figure 14. Graphical summary of the CLS static inhomogeneity, ${\Delta_2}^2/C(0)$, as defined by Eq. 7 for (a) Lenk and (b) Menk with a color scheme to show the trend. See the supplementary material Section S9 for full fits and fit parameters.

Bicelle doping with PE, PG, and PS has been shown, by solid state NMR, to modulate the bicelle's acyl region packing, fluidity, and surface charge, which in turn shifts the balance between the hydrophobic and electrostatic interactions that determine the degree of insertion of enkephalins into the bicelle.[50] The authors found that 10% doping with PE induces significant packing in the lipid's acyl region near the headgroup, which was attributed to the PE's small headgroup size.[50] This packing causes the peptide to be more surface bound,[50] which correlates to a smaller conformational distribution;[51] this therefore leads to a smaller static inhomogeneity observed in the 2D IR time scales.[29] PS and PG, on the other hand, have negatively charged headgroups at neutral pH and are associated with the positively charged N-terminus in zwitterionic enkephalins.[91] The authors of the solid-state NMR study found that 10% doping with PS does not significantly change the bicelle and that the electrostatic interaction with Menk is weaker than in PG.[50] This is consistent with our CLS results, which suggest that the enkephalin conformational distribution in 100% PC bicelles and 10% PS bicelles is similar because the amount of enkephalin static inhomogeneity between PC and PS bicelles is almost identical. The authors found that the greatest perturbation was caused by 10% doping with PG, which significantly increased bicelle fluidity and, through the electrostatic interaction, caused Menk to be surface bound.[50,51] This is also consistent with our CLS results, which show that PG bicelles had the lowest static inhomogeneity, which correlates to a lower conformational distribution, which correlates to a surface bound peptide. Although our results are mostly within experimental error and cannot be used to draw any strong conclusions, the astounding correlation with previously published NMR studies suggests that the tyrosine ring mode is sensitive to small changes in local environment.

V. CONCLUSION

In this work we studied the ultrafast vibrational dynamics of the tyrosine ring mode at long T, up to 10 ps. Our results show that the tyrosine ring mode exhibits rich relaxation dynamics that involve fast vibrational relaxation to one or more dark states. This fast vibrational relaxation occurs because the ring mode is coupled to a large network of lower frequency modes, as evidenced by temperature dependent FTIR and DFT calculations. The ring mode also

exhibits some sensitivity to its local environment. Quantitative analysis was complicated by the presence of a line shape distortion related to vibrational relaxation. We proposed and discussed three models: a population exchange with hot-states model, a local environment dependent IVR rate model, and a coherence transfer model. The latter two models could explain some features of the line shape distortion. Given these distortions, a qualitative analysis was still possible by fitting the CLS data with a formula that includes an underdamped oscillation to extract the static inhomogeneity. In the enkephalin system studied in this work, we hypothesized that the local environment sensitivity was manifest in the tyrosine ring mode's static inhomogeneity, which we attributed to the amount of conformational heterogeneity present in different bicelles. Our qualitative analysis found that mode's static inhomogeneity followed the expected trend based on lipid headgroup size and charge.

As the sensitivity of 2D IR is pushed to its limit, new features will be observable in the spectra. Ideally, these new features would provide a better understanding of a system's dynamics and the system's interaction with its local environment. Recent examples that highlights this point include the identification of a hydrogen-bond sensitive Fermi-resonance[65] or the hydrogen-bond sensitive vibrational relaxation rate.[92] The use and identification of such new features in 2D IR spectroscopy will require a more solid theoretical underpinning. This will likely involve the development of better methods to model vibrational potential energy surfaces, identification of dark states and vibrational relaxation pathways (which may be facilitated by 2D IR experiments with a narrow-band pump and a continuum probe), and the development of simulation protocols that can accurately and efficiently model the effects of local-environments on the potential energy surface.

SUPPLEMENTARY MATERIAL

See supplementary material describing the experimental 2D IR setup; the linear IR data; the anharmonic DFT calculations; the IR pump-probe data, orientational dynamics, and associated fits; the 2D IR data and associated fits; 2D IR spectra of p-cresol in hexanes; line shape distortion of Lenk in buffer; CLS data and the associated fits; computational details for the hot-

states exchange model (the same framework is used for the local environment dependent IVR model).

ACKNOWLEDGMENTS

This research was supported by grants from the U.S. National Science Foundation (CHE-1310693, CHE-1013071, and CHE-1905395). We acknowledge shared instrumentation supported by NSF grants (CHE-0802913 and CHE-1414466) and the use of the UC Irvine Laser Spectroscopy Labs. We want to thank Professor Vartkess A. Apkarian for helpful discussion on the coherence transfer model and Professor Christopher M. Cheatum for helpful discussion on the local environment dependent IVR model. We are also grateful to Dr. Hiroaki Maekawa for his help with laser maintenance. C.G. and N.S.U. acknowledge the support of UC Irvine SURP and UROP fellowships.

DATA AVAILABILITY

The data that support the findings of this study are available within the article and its supplementary material as well as from the corresponding author upon reasonable request.

References

[1] H. Kim and M. Cho, "Infrared Probes for Studying the Structure and Dynamics of Biomolecules," *Chem. Rev.* **113**, 5817 (2013).

[2] J. Ma, I. M. Pazos, W. Zhang, R. M. Culik, and F. Gai, "Site-Specific Infrared Probes of Proteins," *Annu. Rev. Phys. Chem.* **66**, 357 (2015).

[3] B. Błasiak, C. H. Londergan, L. J. Webb, and M. Cho, "Vibrational Probes: From Small Molecule Solvatochromism Theory and Experiments to Applications in Complex Systems," *Acc. Chem. Res.* **50**, 968 (2017).

[4] R. Adhikary, J. Zimmermann, and F. E. Romesberg, "Transparent Window Vibrational Probes for the Characterization of Proteins With High Structural and Temporal Resolution," *Chem. Rev.* **117**, 1927 (2017).

[5] A. Ghosh, J. S. Ostrander, and M. T. Zanni, "Watching Proteins Wiggle: Mapping Structures with Two-Dimensional Infrared Spectroscopy," *Chem. Rev.* **117**, 10726 (2017).

[6] A. M. Woys, S. S. Mukherjee, D. R. Skoff, S. D. Moran, and M. T. Zanni, "A Strongly Absorbing Class of Non-Natural Labels for Probing Protein Electrostatics and Solvation with FTIR and 2D IR Spectroscopies," *J. Phys. Chem. B* **117**, 5009 (2013).

[7] L. J. G. W. van Wilderen, D. Kern-Michler, H. M. Müller-Werkmeister, and J. Bredenbeck, "Vibrational dynamics and solvatochromism of the label SCN in various solvents and hemoglobin by time dependent IR and 2D-IR spectroscopy," *Phys. Chem. Chem. Phys.* **16**, 19643 (2014).
[8] C. Zanobini, O. Bozovic, B. Jankovic, K. L. Koziol, P. J. M. Johnson, P. Hamm, A. Gulzar, S. Wolf, and G. Stock, "Azidohomoalanine: A Minimally Invasive, Versatile, and Sensitive Infrared Label in Proteins To Study Ligand Binding," *J. Phys. Chem. B* **122**, 10118 (2018).
[9] S. R. Dalton, A. R. Vienneau, S. R. Burstein, R. J. Xu, S. Linse, and C. H. Londergan, "Cyanylated Cysteine Reports Site-Specific Changes at Protein–Protein-Binding Interfaces Without Perturbation," *Biochemistry* **57**, 3702 (2018).
[10] G. Lee, D. Kossowska, J. Lim, S. Kim, H. Han, K. Kwak, and M. Cho, "Cyanamide as an Infrared Reporter: Comparison of Vibrational Properties between Nitriles Bonded to N and C Atoms," *J. Phys. Chem. B* **122**, 4035 (2018).
[11] S. Ramos, R. E. Horness, J. A. Collins, D. Haak, and M. C. Thielges, "Site-specific 2D IR spectroscopy: a general approach for the characterization of protein dynamics with high spatial and temporal resolution," *Phys. Chem. Chem. Phys.* **21**, 780 (2019).
[12] T. Brinzer and S. Garrett-Roe, "Temperature and chain length dependence of ultrafast vibrational dynamics of thiocyanate in alkylimidazolium ionic liquids: A random walk on a rugged energy landscape," *J. Chem. Phys.* **147**, 194501 (2017).
[13] S. A. Yamada, H. E. Bailey, A. Tamimi, C. Li, and M. D. Fayer, "Dynamics in a Room-Temperature Ionic Liquid from the Cation Perspective: 2D IR Vibrational Echo Spectroscopy," *Journal of the American Chemical Society* **139**, 2408 (2017).
[14] S. D. Fried and S. G. Boxer, "Measuring Electric Fields and Noncovalent Interactions Using the Vibrational Stark Effect," *Acc. Chem. Res.* **48**, 998 (2015).
[15] J. D. Slocum and L. J. Webb, "Measuring Electric Fields in Biological Matter Using the Vibrational Stark Effect of Nitrile Probes," *Annu. Rev. Phys. Chem.* **69**, 253 (2018).
[16] V. P. Roy and K. J. Kubarych, "Interfacial Hydration Dynamics in Cationic Micelles Using 2D-IR and NMR," *J. Phys. Chem. B* **121**, 9621 (2017).
[17] D. G. Osborne, J. A. Dunbar, J. G. Lapping, A. M. White, and K. J. Kubarych, "Site-Specific Measurements of Lipid Membrane Interfacial Water Dynamics with Multidimensional Infrared Spectroscopy," *J. Phys. Chem. B* **117**, 15407 (2013).
[18] C. Yan, J. E. Thomaz, Y.-L. Wang, J. Nishida, R. Yuan, J. P. Breen, and M. D. Fayer, "Ultrafast to Ultraslow Dynamics of a Langmuir Monolayer at the Air/Water Interface Observed with Reflection Enhanced 2D IR Spectroscopy," *Journal of the American Chemical Society* **139**, 16518 (2017).
[19] C. R. Baiz, B. Błasiak, J. Bredenbeck, M. Cho, J.-H. Choi, S. A. Corcelli, A. G. Dijkstra, C.-J. Feng, S. Garrett-Roe, N.-H. Ge, M. W. D. Hanson-Heine, J. D. Hirst, T. L. C. Jansen, K. Kwac, K. J. Kubarych, C. H. Londergan, H. Maekawa, M. Reppert, S. Saito, S. Roy, J. L. Skinner, G. Stock, J. E. Straub, M. C. Thielges, K. Tominaga, A. Tokmakoff, H. Torii, L. Wang, L. J. Webb, and M. T. Zanni, "Vibrational Spectroscopic Map, Vibrational Spectroscopy, and Intermolecular Interaction," *Chem. Rev.* **120**, 7152 (2020).
[20] M. Maj, C. Ahn, B. Błasiak, K. Kwak, H. Han, and M. Cho, "Isonitrile as an Ultrasensitive Infrared Reporter of Hydrogen-Bonding Structure and Dynamics," *J. Phys. Chem. B* **120**, 10167 (2016).
[21] M. P. Wolfshorndl, R. Baskin, I. Dhawan, and C. H. Londergan, "Covalently Bound Azido Groups Are Very Specific Water Sensors, Even in Hydrogen-Bonding Environments," *J. Phys. Chem. B* **116**, 1172 (2012).
[22] M. Maj, C. Ahn, D. Kossowska, K. Park, K. Kwak, H. Han, and M. Cho, "β-Isocyanoalanine as an IR probe: comparison of vibrational dynamics between isonitrile and nitrile-derivatized IR probes," *Phys. Chem. Chem. Phys.* **17**, 11770 (2015).

[23] S. J. Miyake-Stoner, C. A. Refakis, J. T. Hammill, H. Lusic, J. L. Hazen, A. Deiters, and R. A. Mehl, "Generating Permissive Site-Specific Unnatural Aminoacyl-tRNA Synthetases," *Biochemistry* **49**, 1667 (2010).
[24] I. Peran, T. Oudenhoven, A. M. Woys, M. D. Watson, T. O. Zhang, I. Carrico, M. T. Zanni, and D. P. Raleigh, "General Strategy for the Bioorthogonal Incorporation of Strongly Absorbing, Solvation-Sensitive Infrared Probes into Proteins," *J. Phys. Chem. B* **118**, 7946 (2014).
[25] I. A. Ahmed and F. Gai, "Simple method to introduce an ester infrared probe into proteins," *Protein Sci.* **26**, 375 (2017).
[26] E. M. Tookmanian, E. E. Fenlon, and S. H. Brewer, "Synthesis and protein incorporation of azido-modified unnatural amino acids," *RSC Advances* **5**, 1274 (2015).
[27] F. Chalyavi, P. H. Gilmartin, A. J. Schmitz, M. W. Fennie, and M. J. Tucker, "Synthesis of 5-Cyano-Tryptophan as a Two-Dimensional Infrared Spectroscopic Reporter of Structure," *Angew. Chem. Int. Ed.* **57**, 7528 (2018).
[28] S. Bagchi, C. Falvo, S. Mukamel, and R. M. Hochstrasser, "2D-IR Experiments and Simulations of the Coupling between Amide-I and Ionizable Side Chains in Proteins: Application to the Villin Headpiece," *J. Phys. Chem. B* **113**, 11260 (2009).
[29] S. Sul, Y. Feng, U. Le, D. J. Tobias, and N.-H. Ge, "Interactions of Tyrosine in Leu-Enkephalin at a Membrane−Water Interface: An Ultrafast Two-Dimensional Infrared Study Combined with Density Functional Calculations and Molecular Dynamics Simulations," *J. Phys. Chem. B* **114**, 1180 (2010).
[30] F. Chalyavi, D. G. Hogle, and M. J. Tucker, "Tyrosine as a Non-perturbing Site-Specific Vibrational Reporter for Protein Dynamics," *J. Phys. Chem. B* **121**, 6380 (2017).
[31] F. Chalyavi, A. J. Schmitz, and M. J. Tucker, "Unperturbed Detection of the Dynamic Structure in the Hydrophobic Core of Trp-Cage via Two-Dimensional Infrared Spectroscopy," *J. Phys. Chem. Lett.* **11**, 832 (2020).
[32] A. Ghosh, M. J. Tucker, and R. M. Hochstrasser, "Identification of Arginine Residues in Peptides by 2D-IR Echo Spectroscopy," *J. Phys. Chem. A* **115**, 9731 (2011).
[33] A. Ghosh, M. J. Tucker, and F. Gai, "2D IR Spectroscopy of Histidine: Probing Side-Chain Structure and Dynamics via Backbone Amide Vibrations," *J. Phys. Chem. B* **118**, 7799 (2014).
[34] R. Takahashi and T. Noguchi, "Criteria for Determining the Hydrogen-Bond Structures of a Tyrosine Side Chain by Fourier Transform Infrared Spectroscopy: Density Functional Theory Analyses of Model Hydrogen-Bonded Complexes of p-Cresol," *J. Phys. Chem. B* **111**, 13833 (2007).
[35] B. Hernández, F. Pflüger, A. Adenier, S. G. Kruglik, and M. Ghomi, "Vibrational Analysis of Amino Acids and Short Peptides in Hydrated Media. VIII. Amino Acids with Aromatic Side Chains: l-Phenylalanine, l-Tyrosine, and l-Tryptophan," *J. Phys. Chem. B* **114**, 15319 (2010).
[36] Y. N. Chirgadze, O. V. Fedorov, and N. P. Trushina, "Estimation of amino acid residue side-chain absorption in the infrared spectra of protein solutions in heavy water," *Biopolymers* **14**, 679 (1975).
[37] A. Barth, "The infrared absorption of amino acid side chains," *Prog. Biophys. Mol. Biol.* **74**, 141 (2000).
[38] K. J. Rothschild, P. Roepe, P. L. Ahl, T. N. Earnest, R. A. Bogomolni, S. K. Das Gupta, C. M. Mulliken, and J. Herzfeld, "Evidence for a tyrosine protonation change during the primary phototransition of bacteriorhodopsin at low temperature," *Proc. Nat. Acad. Sci.* **83**, 347 (1986).
[39] T. Noguchi, Y. Inoue, and X.-S. Tang, "Structural Coupling between the Oxygen-Evolving Mn Cluster and a Tyrosine Residue in Photosystem II As Revealed by Fourier Transform Infrared Spectroscopy," *Biochemistry* **36**, 14705 (1997).
[40] P. Hellwig, U. Pfitzner, J. Behr, B. Rost, R. P. Pesavento, W. v. Donk, R. B. Gennis, H. Michel, B. Ludwig, and W. Mäntele, "Vibrational Modes of Tyrosines in Cytochrome c Oxidase from Paracoccus denitrificans: FTIR and Electrochemical Studies on Tyr-D4-labeled and on Tyr280His and Tyr35Phe Mutant Enzymes," *Biochemistry* **41**, 9116 (2002).

[41] H. Fabian, C. Schultz, J. Backmann, U. Hahn, W. Saenger, H. H. Mantsch, and D. Naumann, "Impact of Point Mutations on the Structure and Thermal Stability of Ribonuclease T1 in Aqueous Solution Probed by Fourier Transform Infrared Spectroscopy," *Biochemistry* **33**, 10725 (1994).
[42] S. Tremmel, M. Beyermann, H. Oschkinat, M. Bienert, D. Naumann, and H. Fabian, "13C-Labeled Tyrosine Residues as Local IR Probes for Monitoring Conformational Changes in Peptides and Proteins," *Angew. Chem. Int. Ed.* **44**, 4631 (2005).
[43] Y. Feng, I. Vinogradov, and N.-H. Ge, "General noise suppression scheme with reference detection in heterodyne nonlinear spectroscopy," *Opt. Express* **25**, 26262 (2017).
[44] Y. Feng, I. Vinogradov, and N.-H. Ge, "Optimized noise reduction scheme for heterodyne spectroscopy using array detectors," *Opt. Express* **27**, 20323 (2019).
[45] J. Hughes, T. W. Smith, H. W. Kosterlitz, L. A. Fothergill, B. A. Morgan, and H. R. Morris, "Identification of two related pentapeptides from the brain with potent opiate agonist activity," *Nature* **258**, 577 (1975).
[46] D. F. Sargent and R. Schwyzer, "Membrane lipid phase as catalyst for peptide-receptor interactions," *Proc. Nat. Acad. Sci.* **83**, 5774 (1986).
[47] T. Takekiyo, M. Kato, and Y. Taniguchi, "FT-IR spectroscopic study on conformational equilibria of [Leu]5-enkephalin in DMSO and 2H2O solutions," *J. Mol. Liq.* **119**, 147 (2005).
[48] S.-L. Han, E. R. Stimson, F. R. Maxfield, and H. A. Scheraga, "CONFORMATIONALSTUDY OF [LEU5]-ENKEPHALIN BY LASER RAMAN SPECTROSCOPY," *Int. J. Pept. Protein Res.* **16**, 173 (1980).
[49] M. Aburi and P. E. Smith, "A conformational analysis of leucine enkephalin as a function of pH," *Biopolymers* **64**, 177 (2002).
[50] I. Marcotte, E. J. Dufourc, M. Ouellet, and M. Auger, "Interaction of the Neuropeptide Met-Enkephalin with Zwitterionic and Negatively Charged Bicelles as Viewed by 31P and 2H Solid-State NMR," *Biophys. J.* **85**, 328 (2003).
[51] I. Marcotte, F. Separovic, M. Auger, and S. M. Gagné, "A Multidimensional ¹H NMR Investigation of the Conformation of Methionine-Enkephalin in Fast-Tumbling Bicelles," *Biophys. J.* **86**, 1587 (2004).
[52] H. I. Mosberg, R. Hurst, V. J. Hruby, K. Gee, H. I. Yamamura, J. J. Galligan, and T. F. Burks, "Bis-penicillamine enkephalins possess highly improved specificity toward delta opioid receptors," *Proc. Nat. Acad. Sci.* **80**, 5871 (1983).
[53] V. J. Hruby, L. F. Kao, B. M. Pettitt, and M. Karplus, "The conformational properties of the delta opioid peptide [cyclic] [D-pen2,D-pen5]enkephalin in aqueous solution determined by NMR and energy minimization calculations," *Journal of the American Chemical Society* **110**, 3351 (1988).
[54] H. W. Kosterlitz, J. A. H. Lord, S. J. Paterson, and A. A. Waterfield, "Effects of changes in the structure of enkephalins and of narcotic analgesic drugs on their interactions with μ and δ-receptors," *Br. J. Pharmacol.* **68**, 333 (1980).
[55] A. Milon, T. Miyazawa, and T. Higashijima, "Transferred nuclear Overhauser effect analyses of membrane-bound enkephalin analogs by proton nuclear magnetic resonance: correlation between activities and membrane-bound conformations," *Biochemistry* **29**, 65 (1990).
[56] C. M. Deber and B. A. Behnam, "Role of membrane lipids in peptide hormone function: binding of enkephalins to micelles," *Proc. Nat. Acad. Sci.* **81**, 61 (1984).
[57] C. Yang, S. Peng, Q. Xie, J. Peng, J. Wei, and Y. Hu. "FTIR spectral subtraction based on asymmetric least squares"; 2011 4th International Conference on Biomedical Engineering and Informatics (BMEI), 2011.
[58] S.-H. Shim and M. T. Zanni, "How to turn your pump–probe instrument into a multidimensional spectrometer: 2D IR and Vis spectroscopiesvia pulse shaping," *Phys. Chem. Chem. Phys.* **11**, 748 (2009).

[59] M. J. Frisch, G. W. Trucks, H. B. Schlegel, G. E. Scuseria, M. A. Robb, J. R. Cheeseman, J. A. Montgomery, T. Vreven, K. N. Kudin, J. C. Burant, J. M. Millam, S. S. Iyengar, J. Tomasi, V. Barone, B. Mennucci, M. Cossi, G. Scalmani, N. Rega, G. A. Petersson, H. Nakatsuji, M. Hada, M. Ehara, K. Toyota, R. Fukuda, J. Hasegawa, M. Ishida, T. Nakajima, Y. Honda, O. Kitao, H. Nakai, M. Klene, X. Li, J. E. Knox, H. P. Hratchian, J. B. Cross, V. Bakken, C. Adamo, J. Jaramillo, R. Gomperts, R. E. Stratmann, O. Yazyev, A. J. Austin, R. Cammi, C. Pomelli, J. W. Ochterski, P. Y. Ayala, K. Morokuma, G. A. Voth, P. Salvador, J. J. Dannenberg, V. G. Zakrzewski, S. Dapprich, A. D. Daniels, M. C. Strain, O. Farkas, D. K. Malick, A. D. Rabuck, K. Raghavachari, J. B. Foresman, J. V. Ortiz, Q. Cui, A. G. Baboul, S. Clifford, J. Cioslowski, B. B. Stefanov, G. Liu, A. Liashenko, P. Piskorz, I. Komaromi, R. L. Martin, D. J. Fox, T. Keith, A. Laham, C. Y. Peng, A. Nanayakkara, M. Challacombe, P. M. W. Gill, B. Johnson, W. Chen, M. W. Wong, C. Gonzalez, and J. A. Pople. Gaussian 03, Revision C.01, 2003.

[60] K.-K. Lee, K.-H. Park, J.-H. Choi, J.-H. Ha, S.-J. Jeon, and M. Cho, "Ultrafast Vibrational Spectroscopy of Cyanophenols," *J. Phys. Chem. A* **114**, 2757 (2010).

[61] H. Maekawa and N.-H. Ge, "Picosecond Rotational Interconversion Adjacent to a C═O Bond Studied by Two-Dimensional Infrared Spectroscopy," *J. Phys. Chem. B* **116**, 11292 (2012).

[62] K.-H. Park, J. Jeon, Y. Park, S. Lee, H.-J. Kwon, C. Joo, S. Park, H. Han, and M. Cho, "Infrared Probes Based on Nitrile-Derivatized Prolines: Thermal Insulation Effect and Enhanced Dynamic Range," *J. Phys. Chem. Lett.* **4**, 2105 (2013).

[63] J. M. Rodgers, W. Zhang, C. G. Bazewicz, J. Chen, S. H. Brewer, and F. Gai, "Kinetic Isotope Effect Provides Insight into the Vibrational Relaxation Mechanism of Aromatic Molecules: Application to Cyano-phenylalanine," *J. Phys. Chem. Lett.* **7**, 1281 (2016).

[64] W. Zhang, B. N. Markiewicz, R. S. Doerksen, I. I. I. A. B. Smith, and F. Gai, "C N stretching vibration of 5-cyanotryptophan as an infrared probe of protein local environment: what determines its frequency?," *Phys. Chem. Chem. Phys.* **18**, 7027 (2016).

[65] J. M. Rodgers, R. M. Abaskharon, B. Ding, J. Chen, W. Zhang, and F. Gai, "Fermi resonance as a means to determine the hydrogen-bonding status of two infrared probes," *Phys. Chem. Chem. Phys.* **19**, 16144 (2017).

[66] K. Kwak, S. Park, I. J. Finkelstein, and M. D. Fayer, "Frequency-frequency correlation functions and apodization in two-dimensional infrared vibrational echo spectroscopy: A new approach," *J. Chem. Phys.* **127**, 124503 (2007).

[67] K. Kwak, D. E. Rosenfeld, and M. D. Fayer, "Taking apart the two-dimensional infrared vibrational echo spectra: More information and elimination of distortions," *J. Chem. Phys.* **128**, 204505 (2008).

[68] N.-H. Ge, M. T. Zanni, and R. M. Hochstrasser, "Effects of Vibrational Frequency Correlations on Two-Dimensional Infrared Spectra," *J. Phys. Chem. A* **106**, 962 (2002).

[69] P. Hamm and M. Zanni. *Concepts and Methods of 2D Infrared Spectroscopy*; Cambridge University Press: Cambridge, 2011.

[70] C. H. Giammanco, P. L. Kramer, S. A. Yamada, J. Nishida, A. Tamimi, and M. D. Fayer, "Coupling of Carbon Dioxide Stretch and Bend Vibrations Reveals Thermal Population Dynamics in an Ionic Liquid," *J. Phys. Chem. B* **120**, 549 (2016).

[71] P. Ramesh and R. F. Loring, "Thermal Population Fluctuations in Two-Dimensional Infrared Spectroscopy Captured with Semiclassical Mechanics," *J. Phys. Chem. B* **122**, 3647 (2018).

[72] M. Khalil, N. Demirdöven, and A. Tokmakoff, "Vibrational coherence transfer characterized with Fourier-transform 2D IR spectroscopy," *J. Chem. Phys.* **121**, 362 (2004).

[73] S. Mukamel. *Principles of Nonlinear Optical Spectroscopy*; Oxford University Press: Oxford, U.K., 1999.

[74] N.-H. Ge and R. M. Hochstrasser, "Femtosecond two-dimensional infrared spectroscopy: IR-COSY and THIRSTY," *PhysChemComm* **5**, 17 (2002).

[75] J. D. Hybl, A. Yu, D. A. Farrow, and D. M. Jonas, "Polar Solvation Dynamics in the Femtosecond Evolution of Two-Dimensional Fourier Transform Spectra," *J. Phys. Chem. A* **106**, 7651 (2002).

[76] Q. Guo, P. Pagano, Y.-L. Li, A. Kohen, and C. M. Cheatum, "Line shape analysis of two-dimensional infrared spectra," *J. Chem. Phys.* **142**, 212427 (2015).
[77] J. C. Owrutsky, D. Raftery, and R. M. Hochstrasser, "Vibrational Relaxation Dynamics in Solutions," *Annu. Rev. Phys. Chem.* **45**, 519 (1994).
[78] V. M. Kenkre, A. Tokmakoff, and M. D. Fayer, "Theory of vibrational relaxation of polyatomic molecules in liquids," *J. Chem. Phys.* **101**, 10618 (1994).
[79] P. Hamm, M. Lim, and R. M. Hochstrasser, "Vibrational energy relaxation of the cyanide ion in water," *J. Chem. Phys.* **107**, 10523 (1997).
[80] R. M. Stratt, "The Instantaneous Normal Modes of Liquids," *Acc. Chem. Res.* **28**, 201 (1995).
[81] M. K. Hazra and B. Bagchi, "Collective excitations in liquid dimethyl sulfoxide (DMSO): FIR spectrum, low frequency vibrational density of states, and ultrafast dipolar solvation dynamics," *J. Chem. Phys.* **146**, 024505 (2017).
[82] P. P. Wiewiór, H. Shirota, and E. W. Caster, Jr., "Aqueous dimethyl sulfoxide solutions: Inter- and intra-molecular dynamics," *J. Chem. Phys.* **116**, 4643 (2002).
[83] H. S. Frank and M. W. Evans, "Free Volume and Entropy in Condensed Systems III. Entropy in Binary Liquid Mixtures; Partial Molal Entropy in Dilute Solutions; Structure and Thermodynamics in Aqueous Electrolytes," *J. Chem. Phys.* **13**, 507 (1945).
[84] Y. L. A. Rezus and H. J. Bakker, "Observation of Immobilized Water Molecules around Hydrophobic Groups," *Phys. Rev. Lett.* **99**, 148301 (2007).
[85] T. M. Raschke and M. Levitt, "Detailed Hydration Maps of Benzene and Cyclohexane Reveal Distinct Water Structures," *J. Phys. Chem. B* **108**, 13492 (2004).
[86] T. M. Raschke and M. Levitt, "Nonpolar solutes enhance water structure within hydration shells while reducing interactions between them," *Proc. Nat. Acad. Sci.* **102**, 6777 (2005).
[87] K. P. Gierszal, J. G. Davis, M. D. Hands, D. S. Wilcox, L. V. Slipchenko, and D. Ben-Amotz, "π-Hydrogen Bonding in Liquid Water," *J. Phys. Chem. Lett.* **2**, 2930 (2011).
[88] A. Choudhary and A. Chandra, "Anisotropic structure and dynamics of the solvation shell of a benzene solute in liquid water from ab initio molecular dynamics simulations," *Phys. Chem. Chem. Phys.* **18**, 6132 (2016).
[89] T. Steiner and G. Koellner, "Hydrogen bonds with π-acceptors in proteins: frequencies and role in stabilizing local 3D structures11Edited by R. Huber," *J. Mol. Biol.* **305**, 535 (2001).
[90] C. R. Baiz, K. J. Kubarych, and E. Geva, "Molecular Theory and Simulation of Coherence Transfer in Metal Carbonyls and Its Signature on Multidimensional Infrared Spectra," *J. Phys. Chem. B* **115**, 5322 (2011).
[91] I. Marcotte, M. Ouellet, and M. Auger, "Insights on the interaction of Met-enkephalin with negatively charged membranes—an infrared and solid-state NMR spectroscopic study," *Chem. Phys. Lipids* **127**, 175 (2004).
[92] J. T. King, J. M. Anna, and K. J. Kubarych, "Solvent-hindered intramolecular vibrational redistribution," *Phys. Chem. Chem. Phys.* **13**, 5579 (2011).

Ultrafast Vibrational Dynamics of the Tyrosine Ring Mode and its Application to Enkephalin Insertion into Phospholipid Membranes as Probed by Two-Dimensional Infrared Spectroscopy

Supplementary Material

Ilya Vinogradov, Yuan Feng, S. K. Karthick Kumar, Chenxu Guo, Nina Saki Udagawa, Nien-Hui Ge*

Department of Chemistry, University of California at Irvine, Irvine, CA, 92697-2025, USA

* To whom correspondence should be addressed.
Email address: nhge@uci.edu
Phone: 949-824-1263
FAX: 949-824-8571

Table of Contents

S1. 2D IR Setup

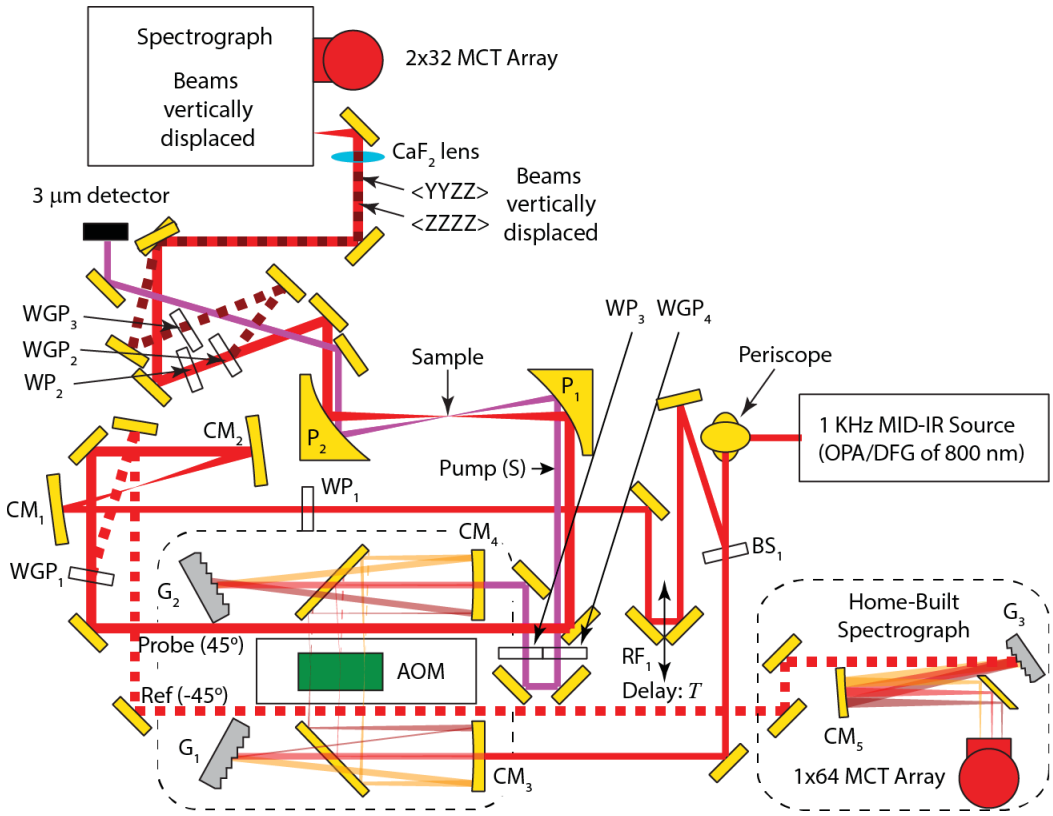

Figure S1: The current state of the 2D IR setup. The beams are labeled as follows. Red: probe; magenta: pump; red-dash: reference. After the sample: red: <ZZZZ>; dark red-dash: <YYZZ>. The optics are labeled as follows. BS: beam splitter; RF: retroreflector; CM: concave mirror; G: grating; WP: ½ waveplate; WGP: wire-grid polarizer; P: parabolic mirror. Boxed in dashed lines are the pulse shaper and the reference spectrograph. This figure is not to scale, but the relative location of all the optics is correct.

Figure S1 shows a schematic of the 2D IR setup. This setup has several notable features. First, the 2D IR setup is equipped with our new smart referencing algorithm.[1,2] Second, the pump double-pulse is generated by a programmable pulse shaper.[3] Third, we use a telescope to enlarge the probe beam to ensure that the probe focus is tighter than the pump focus, which will help generate the largest signal to probe ratio. This is important for maximizing the SNR. Finally, the setup contains polarization control and can collect the <ZZZZ> and <YYZZ> signal polarizations simultaneously.

The polarization scheme is as follows. First, the probe beam is rotated by a ½-waveplate, WP1, to an arbitrary polarization. The first polarizer, WGP_1, is set so that the transmitted beam is linearly polarized at 45° (s + p) at the sample focal spot. The reflected polarization is sent for

reference detection. The reason the ½ waveplate rotation is arbitrary is because this waveplate is used to control the relative intensity between the refence and probe beams. The pump is set to be s-polarized by WGP_2 so that all polarization components of the pump and probe beams in the focal spot volume are either perfectly orthogonal or parallel to each other. The probe at the focal spot volume has both s and p polarizations. The analyzer (WGP_2) is set to the s-polarization, so that s-polarized light is transmitted and so that p-polarized light is reflected. The s-polarization component is rotated by a ½ waveplate (WP_2) to the p-polarization. A small portion of s-polarized light is also reflected, so an additional polarizer (WGP_3) set to p-polarization is used to improve the extinction of the reflected light. The transmitted light corresponds to the <ZZZZ> signal polarization and reflected light corresponds to the <YYZZ> signal polarization. Note that linear polarization is carefully maintained after the first polarizer by using unprotected gold mirrors until the analyzer to prevent the unwanted generation of elliptical polarizations.[4] Finally, we use a set of vertically-displaced mirrors to direct the beams to cross around 115 mm before a f = 100 mm CaF_2 lens (focal length reported for 588 nm) before the entrance slit. The data is acquired by a 2x32 element MCT dual array from Infrared Associates, Inc. using data acquisition equipment from Infrared Systems Development.

As a reference, we also provide some estimates of the mid IR beam parameters used to acquire the 2D IR data in the main text. Our home-built OPA is pumped by 1.2 W of 800 nm light with a FWHM bandwidth of approximately 15 nm. Immediately after the DFG stage, approximately 3 μJ of 6.6 μm mid IR light is generated with a pulse duration estimated at 170 fs. While the 2D IR spectrometer is purged to minimize water vapor absorption, the pulse energy before the pulse shaper is reduced to 1.9 μJ. After the pulse shaper, each pump pulse has an approximate energy of 125 nJ (or 500 nJ total without time delay) at small τ when double pulse falloff is negligible. With good alignment, we can achieve an approximately 150 μm focal spot FWHM for the pump and 75 μm for the probe. This corresponds to a peak intensity of 2.7 GW/cm^2 for each pump pulse at the sample.

S2. FTIR Spectra

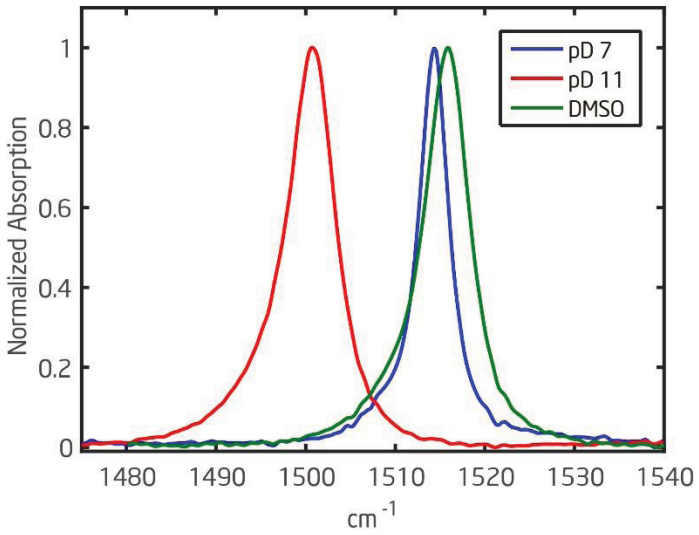

Figure S2: Normalized FTIR data for p-cresol in DMSO and in pD 7 and pD 11 deuterated phosphate buffer at room temperature.

Figure S2 shows the FTIR spectra of p-cresol in pD 7 phospahte buffer and DMSO and its anion in pD 11 phosphate buffer. It is worth noting that the linewidth of p-cresol in DMSO is wider than that in pD 7 buffer. Our pump-probe results show that the vibrationally excited state of p-cresol in DMSO has a faster IVR energy transfer time as compared to in D_2O. Therefore, lifetime broadening is a contributing factor to the larger linewidth. In addition, tyrosine has a similar broadening effect in DMSO vs. D_2O.[5] The authors of that work found that inhomogeneous broadening is also a significant contributor to the larger linewidth of tyrosine in DMSO.

In addition, we provide the unnormalized FTIR spectra, after solvent subtraction and water line removal, used in this work in Figure S3 through Figure S5. All data was taken with a 25 µm spacer. Peptides in bicelles were prepared with a target concentration of 30 mM in all data sets. Peptides in pD 7 buffer had a target concentration of 40 mM concentration. p-Cresol had a concentration of 40 mM in all data sets.

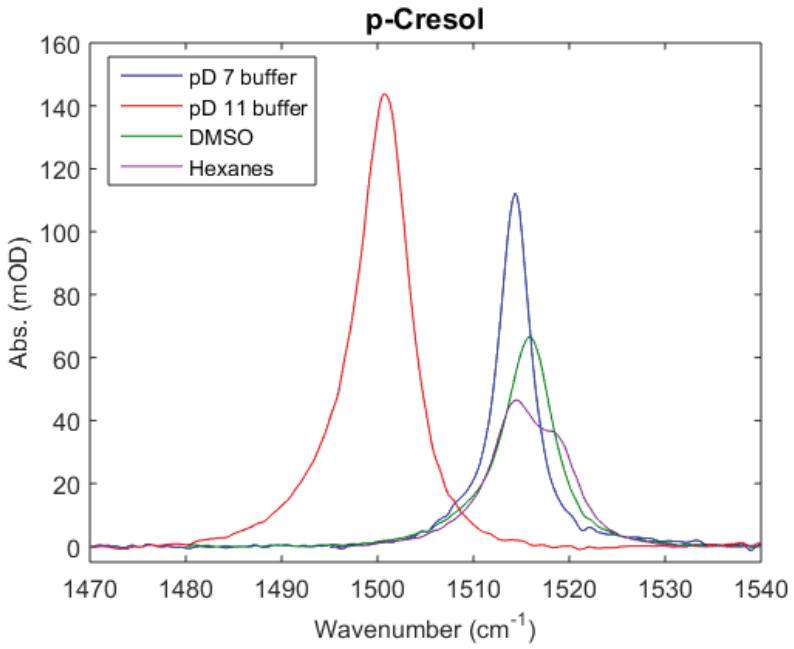

Figure S3: Unnormalized FTIR spectra of p-cresol in various solvents.

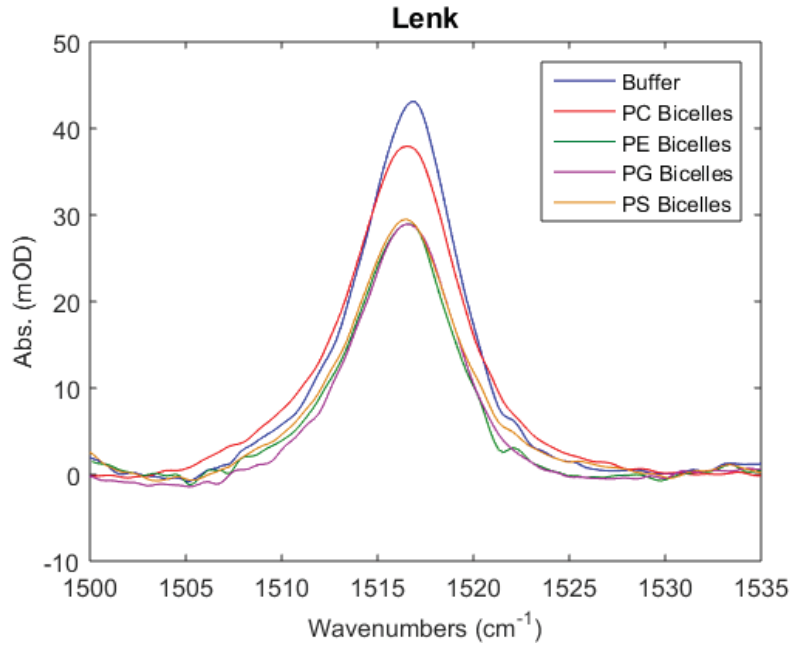

Figure S4: Unnormalized FTIR spectra of Lenk in pD 7 buffer and in bicelles with different doping headgroups.

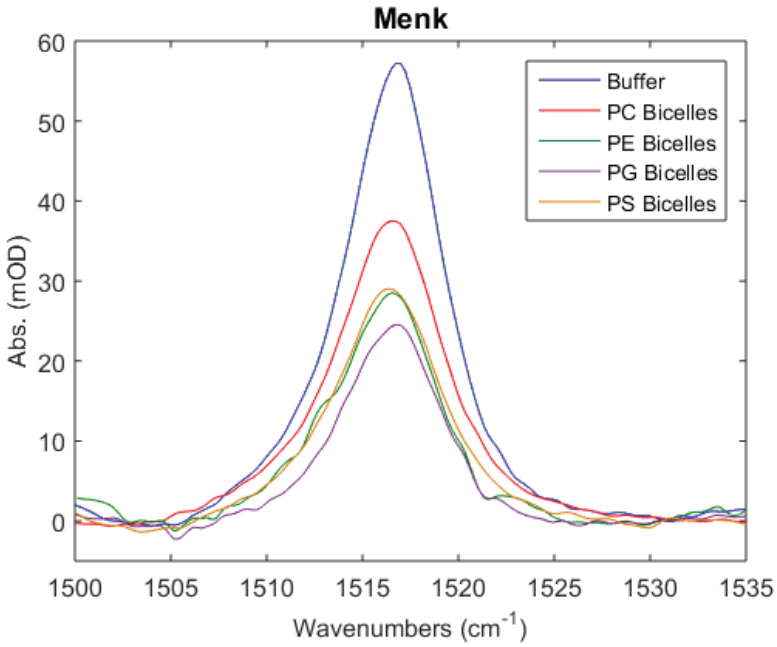

Figure S5: Unnormalized FTIR spectra of Menk in pD 7 buffer and in bicelles with different doping headgroups.

S3. DFT Results

Figure S6 provides a brief summary of our DFT (B3LYP 6-31g+ (d,p)) results on p-cresol-OD in vacuo. The upper triangle in the plot represents anharmonic frequency shift Δ_{ij} $(= \omega_{i+j} - \omega_i - \omega_j)$ between two anharmonically coupled modes. The lower triangle is the anharmonic coupling X_{ij} matrix as output by Gaussian 03.[6] The tyrosine ring mode (#32) is labeled in the figure. The corresponding transition frequencies are shown in Table S1 and the strongly coupled modes (Δ_{ij} < -1.5 cm^{-1}) are given in Table S2.

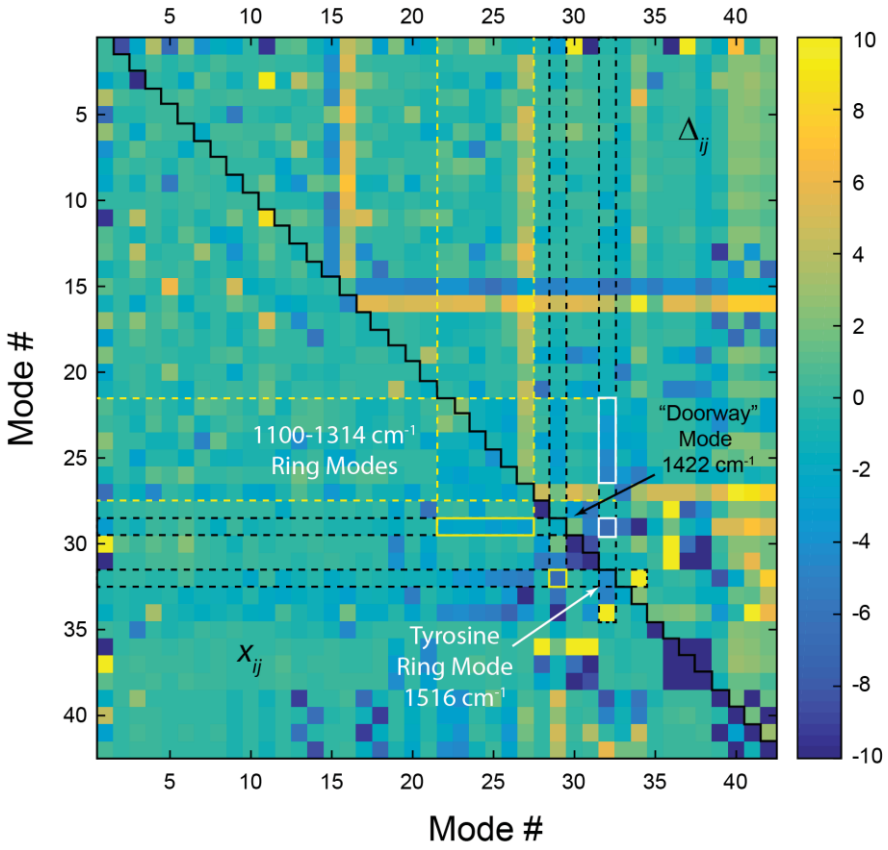

Figure S6. Anharmonic frequency shifts (Δ_{ij}, upper right) and anharmonic couplings (X_{ij}, lower left) for all normal modes in p-cresol-OD. The color bar is in the unit of cm^{-1}.

Table S1. Harmonic and anharmonic frequencies for all normal modes in p-cresol-OD. Energies given in cm^{-1}.

	Harmonic	Anharmonic	Assignment		Harmonic	Anharmonic	Assignment
1	23.4	-114.6	Me rotation	22	1135.6	1121.8	Ring C-H wag (asym.)
2	143	136.1	Me/ring/OD stretch	23	1197.8	1180.1	Ring C-H wag (sym.)
3	235.9	208.1	CCOD dihedral	24	1231.1	1204.4	Methyl-C stretch
4	300.5	303.7	Me/ring/OD bend	25	1277.1	1249.7	C-O stretch
5	331.3	326.5	Me/ring/OD bend	26	1336.4	1314.2	Ring C-H wag
6	410.1	409.1	Me/ring/OD bend	27	1346.8	1308.5	Ring C-C bending
7	421.6	412.8	Ring dihedral	28	1422	1389.7	Ring C-H wag
8	462	457.9	COCOD dihedral	29	1451.7	1422.2	Ring C-H wag
9	514.9	500.7	Ring dihedral	30	1490.9	1463.2	Methyl wag
10	655	647.7	Ring bend	31	1503.2	1459.4	Methyl wag
11	696.4	708.7	Ring dihedral	32	1550.4	1516.3	Ring bend and C-H wag
12	740	730.1	CC/CO stretch	33	1632.1	1592.5	Ring C-C stretch
13	812.5	797.6	C-H dihedral	34	1664.9	1626.6	Ring C-C stretch
14	835	819	C-H dihedral	35	2787.8	2685.6	O-D stretch
15	847.1	845.2	C-H dihedral	36	3031.5	2947.9	Methyl C-H stretch
16	923.7	896.7	COH bend	37	3083.8	2952.1	Methyl C-H stretch
17	932.9	919	C-H dihedral	38	3113.6	2973.1	Methyl C-H stretch
18	966.9	946.4	C-H bend	39	3161.5	3019.8	Ring C-H stretch
19	1008	993.4	Methyl bend	40	3172.7	3032.8	Ring C-H stretch
20	1030.2	1014.5	Ring bend (sym.)	41	3182.7	3049.3	Ring C-H stretch
21	1062.2	1042.8	Methyl wag	42	3208.1	3077.3	Ring C-H stretch

Table S2. Combination band frequencies with mode #32, the 1516 cm^{-1} ring mode, for modes that have a corresponding anharmonic frequency shift greater than 1.5 cm^{-1}. The first entry is the overtone for mode #32. Energies are in units of cm^{-1}.

	Anharmonic Frequency	Combination Band Frequency With Mode #32	Anharmonic Shift Δ_{ij}
32	1516.3	3023.8	-8.7
29	1422.2	2931.9	-6.6
26	1314.2	2825.6	-4.9
25	1249.7	2761.5	-4.5
24	1204.4	2717.3	-3.4
23	1180.1	2692.7	-3.7
22	1121.8	2636.2	-1.9
15	845.2	2355.3	-6.1
12	730.1	2244.4	-1.9
10	647.7	2161.6	-2.4

S4. Pump Probe Data

We also collected polarization-resolved pump probe data for all samples. Figure S7 and Figure S8 show the lifetimes collected as <ZZZZ>+2<YYZZ> with our polarization resolved 2D IR spectrometer. One may fit the peaks to decaying exponentials to extract the vibrational lifetimes. Note that the $v = 0 \rightarrow 1$ transition will experience double exponential behavior because of the contribution from the excited state decay and ground state bleach recovery. To improve the robustness of the fit, the $v = 1 \rightarrow 2$ peak was first fit to a single exponential (right column of the figure) with a time constant τ_1. The time constant of this exponential represents the lifetime of the first excited state, including the IVR contribution. The $v = 0 \rightarrow 1$ peak was then fit to two exponentials (left column of the figure), one of which had the time constant fixed to that of the $v = 1 \rightarrow 2$ peak. The functional form of the fit function is:

$$f(T) = A_1 e^{-\frac{T}{\tau_1}} + A_2 e^{-\frac{T}{\tau_2}} \quad (S1)$$

In addition, we performed the fit starting from 300 fs to avoid the strong coherence artifact present around time zero in our data. The fitting results are summarized in Table S3. The longer time constant represents the decay of the bleach, which coincides with the decay of the IVR peak.

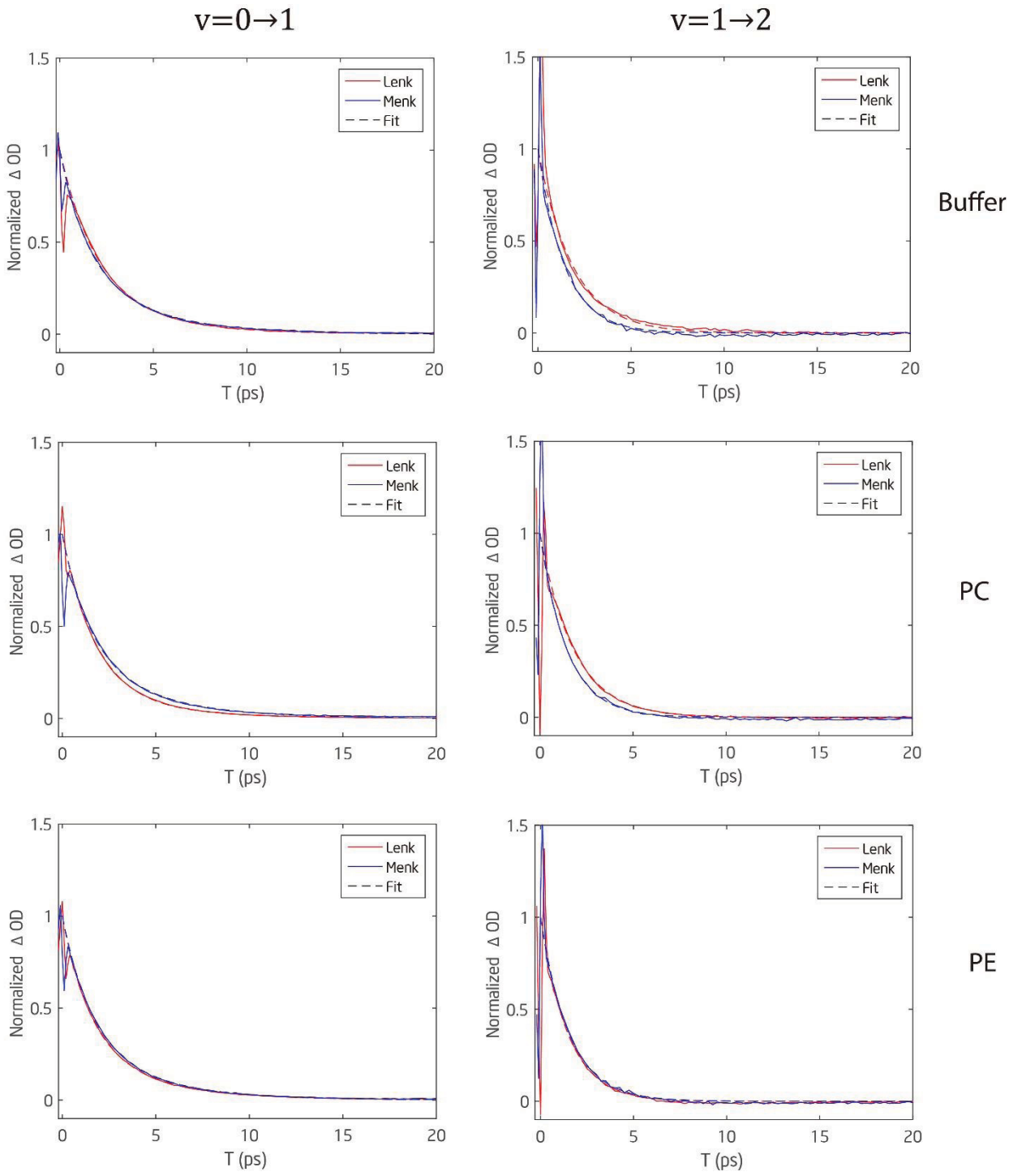

Figure S7. Part 1 of the pump probe data for Lenk and Menk in pD 7 buffer and bicelles. The $v = 0 \rightarrow 1$ peak is at 1517 cm^{-1} and $v = 1 \rightarrow 2$ peak at 1505 cm^{-1}.

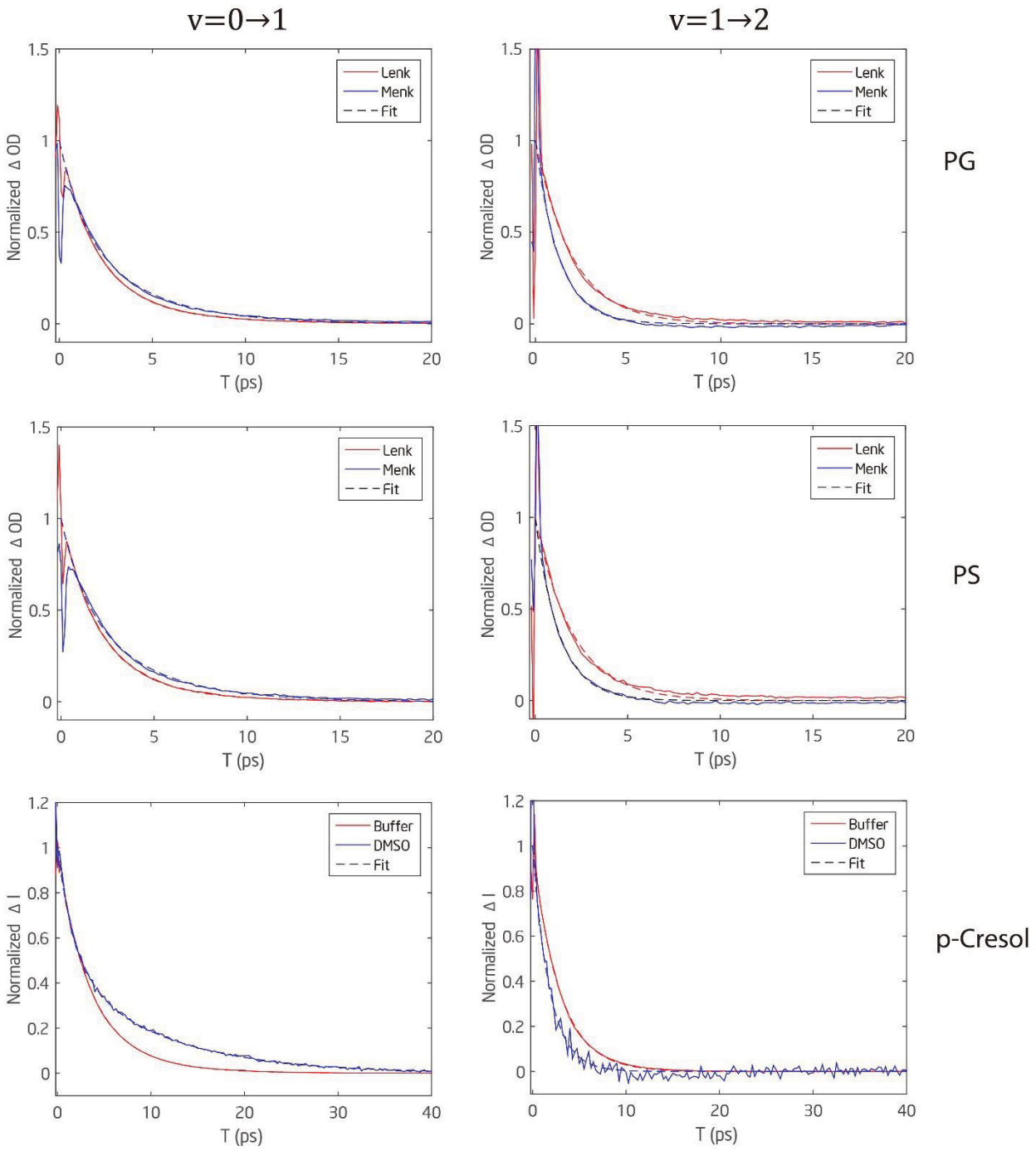

Figure S8. Part 2 of the pump probe data for Lenk and Menk in bicelles, and p-cresol in solvents. The traces shown are at 1517 cm^{-1} for the $v = 0 \rightarrow 1$ peak and 1505 cm^{-1} for the $v = 1 \rightarrow 2$ peak for Lenk and Menk. For p-cresol in pD 7 buffer, the traces are at 1515 cm^{-1} and 1503 cm^{-1}, respectively. For p-cresol in DMSO, the traces are at 1517 cm^{-1} and 1500 cm^{-1}.

Table S3. Double exponential fitting parameters obtained from the pump probe data, with parameters defined by Eq. S1. All buffers in the table are pD 7.

		A_1/A_2	τ_1 (ps)	τ_2 (ps)
Lenk	Buffer	2.5	1.9	3.9
	PC	2.0	1.5	4.0
	PG	6.9	2.0	4.9
	PE	1.5	1.5	4.0
	PS	0.7	1.3	3.8
Menk	Buffer	10.3	1.8	5.8
	PC	7.8	2.0	5.6
	PG	1.5	1.4	3.9
	PE	1.9	1.5	4.1
	PS	0.7	1.3	3.8
p-Cresol	Buffer	1.7	2.8	5.4
	DMSO	1.1	1.8	10.3

S5. Reorientation Dynamics

Figure S9 shows the vibrational anisotropy for p-cresol in pD 7 buffer. The decay happens with a time constant of approximately 8 ps with an offset of 0.27. The vibrational lifetime is less than 3 ps for all samples. Because p-cresol is the smallest molecule we measured, we do not expect reorientation dynamics to be significant in the 2D data of the peptides.

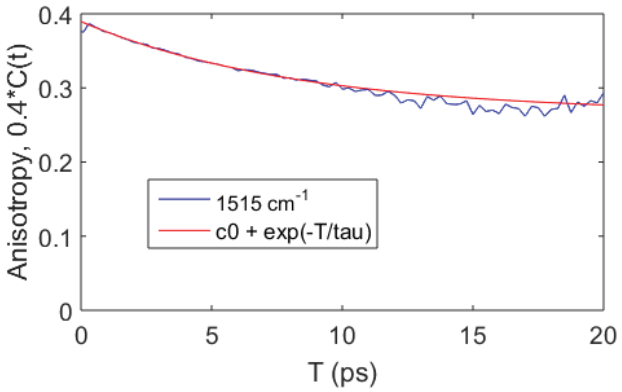

Figure S9. Pump-probe vibrational anisotropy of p-cresol in pD 7 buffer measured at 1515 cm^{-1} (blue) and the fitting with an exponential decay and an offset (red).

S6. 2D IR Response Function Fitting

Spectral fitting is performed by using MATLAB's non-linear least squares optimization function, lsqnonlin. Due to the overparameterization of the model, we tried to use an iterative procedure to fit the 2D IR, pump-probe and FTIR spectra to the same parameter set. This idea has its roots on the fact that different measurements have better representations of different information. Unfortunately, the pump-probe data suffers from a strong background signal from the solvent, bicelles, and peptide. This background signal dephases quickly, so it is not as prominent in the 2D spectra. Therefore, we only show the fits from the 2D IR spectra (Figure S10 through Figure S20, the spectra for Lenk in PC bicelles are shown in the main text). The parameters are summarized in Table S4. The symbols and model are defined in the main text, Section IIIC, Figure 6, and Eq. 1. Note that for several parameters, there are sometimes extreme changes between samples even though the fits are visually okay, which is attributed to overparameterization.

In addition, we also include the following two considerations. First, there can be multiple minima present in the fitting parameters. We used the MultiStart class in MATLAB to overcome this issue. This global search algorithm generates multiple initial guesses, each of which are minimized using the nonlinear least squares procedure. This method ensures, at least for our data set, that a global minimum is always found. Note that if each run consistently finds different local minima, it is likely the least squares convergence criteria is not tight enough. We adjust the convergence criteria when this situation occurred. Second, we included a 0.8 cm^{-1} frequency correction for the pump axis which is related to a small pump double pulse delay generation error.[7]

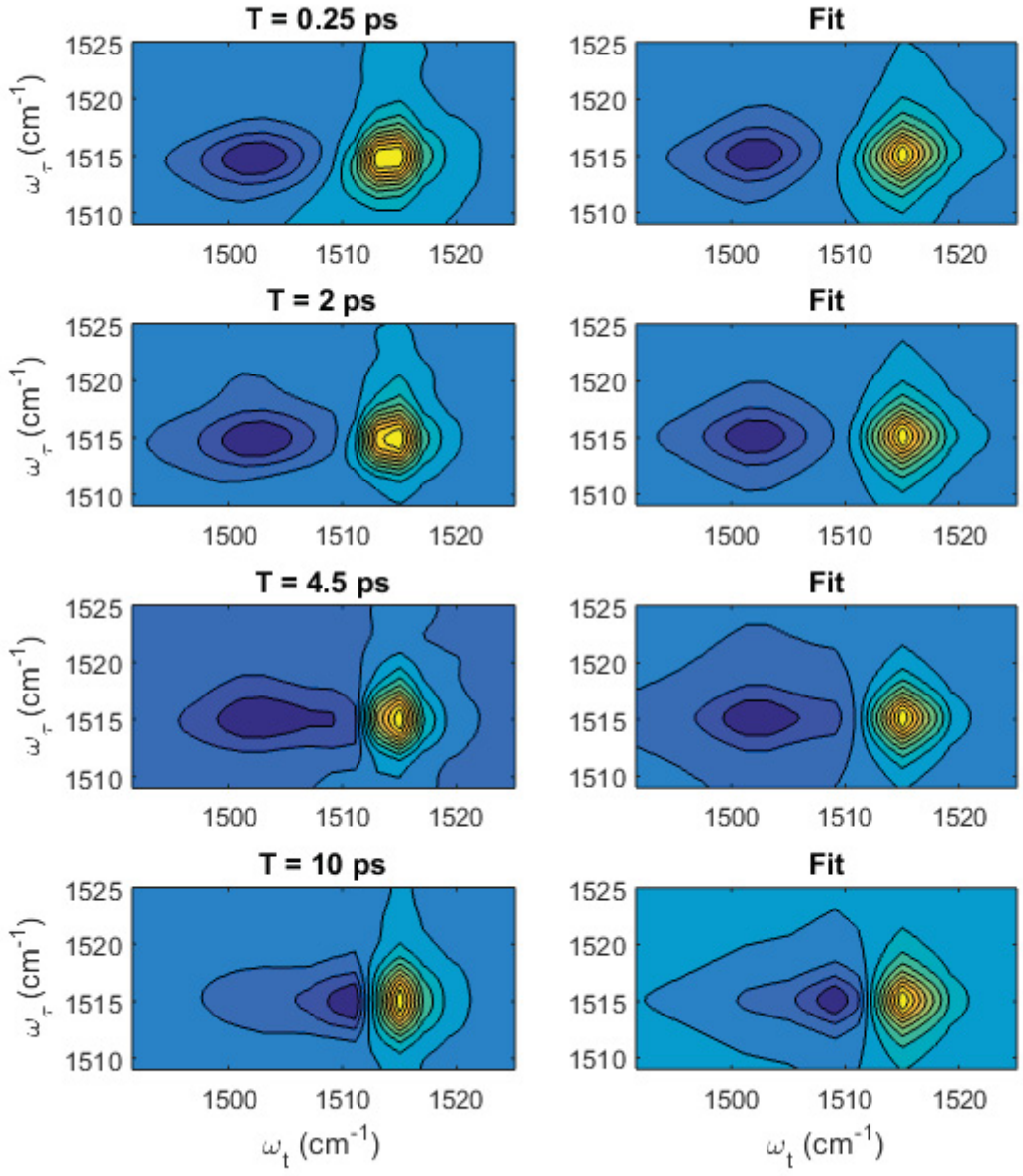

Figure S10. (Left) Experimental 2D IR spectra of p-cresol in pD 7 buffer and (right) response function fitting with the IVR model.

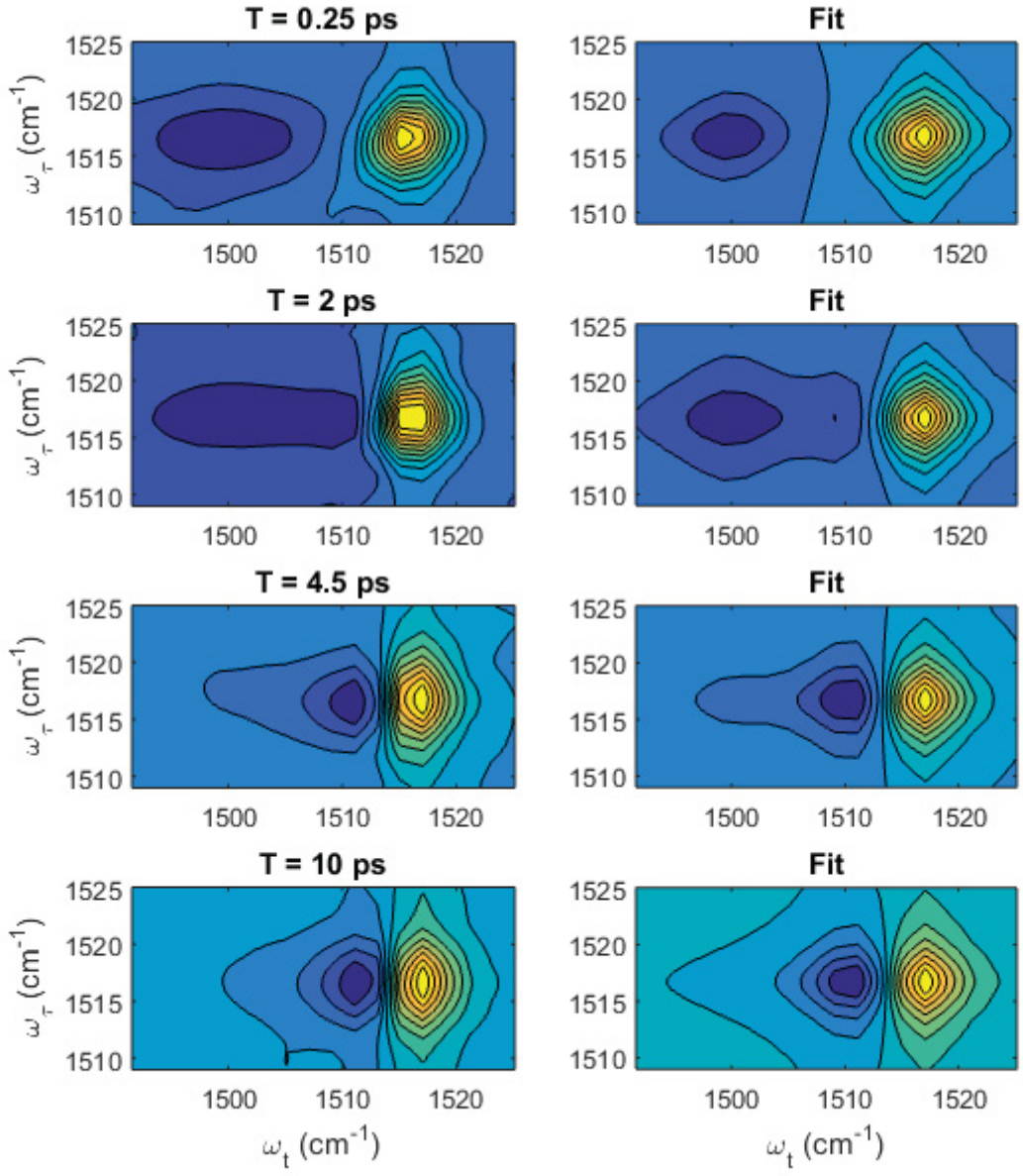

Figure S11. (Left) Experimental 2D IR spectra of p-cresol in DMSO and (right) response function fitting with the IVR model.

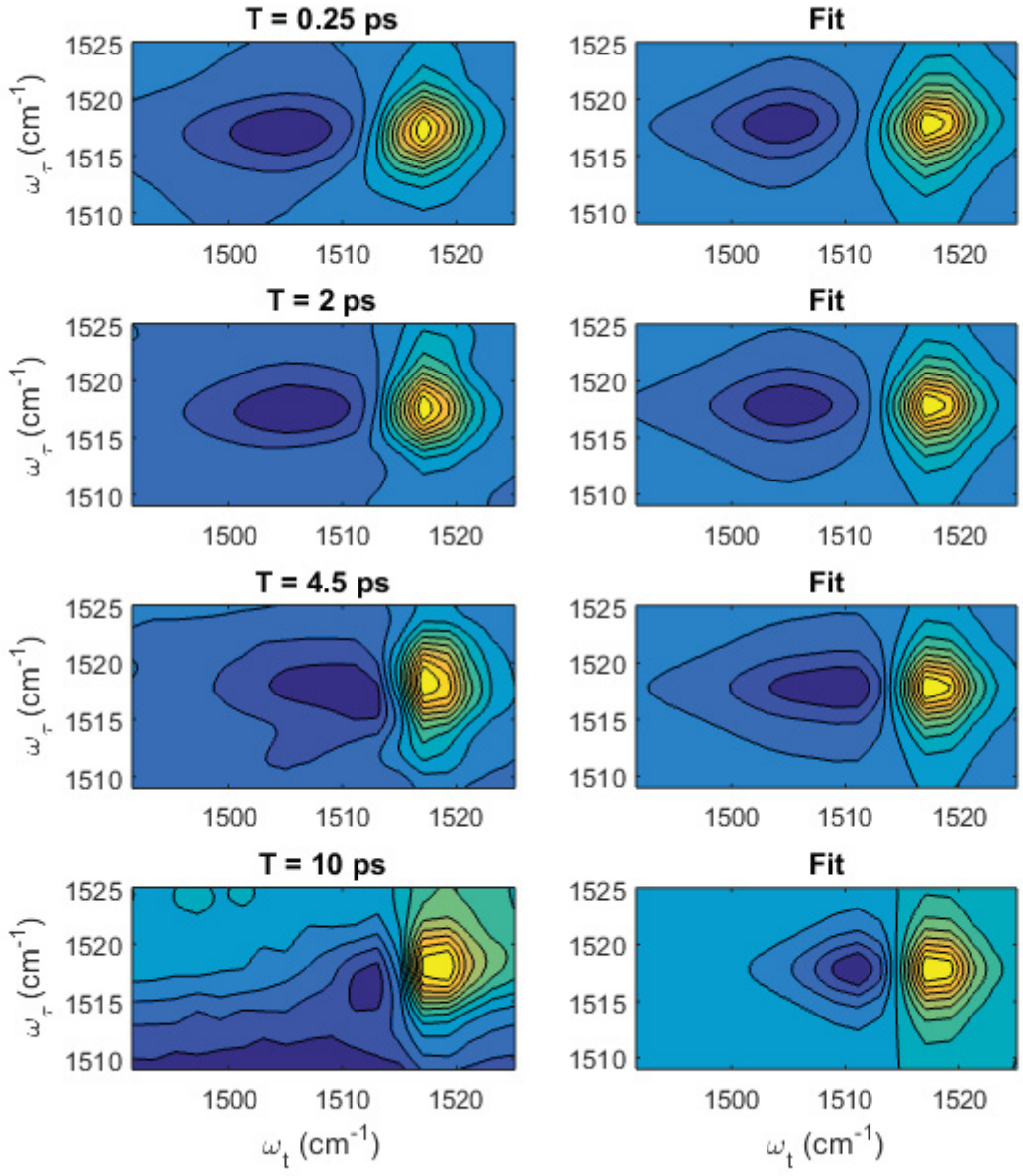

Figure S12. (Left) Experimental 2D IR spectra of Lenk in pD 7 buffer and (right) response function fitting with the IVR model.

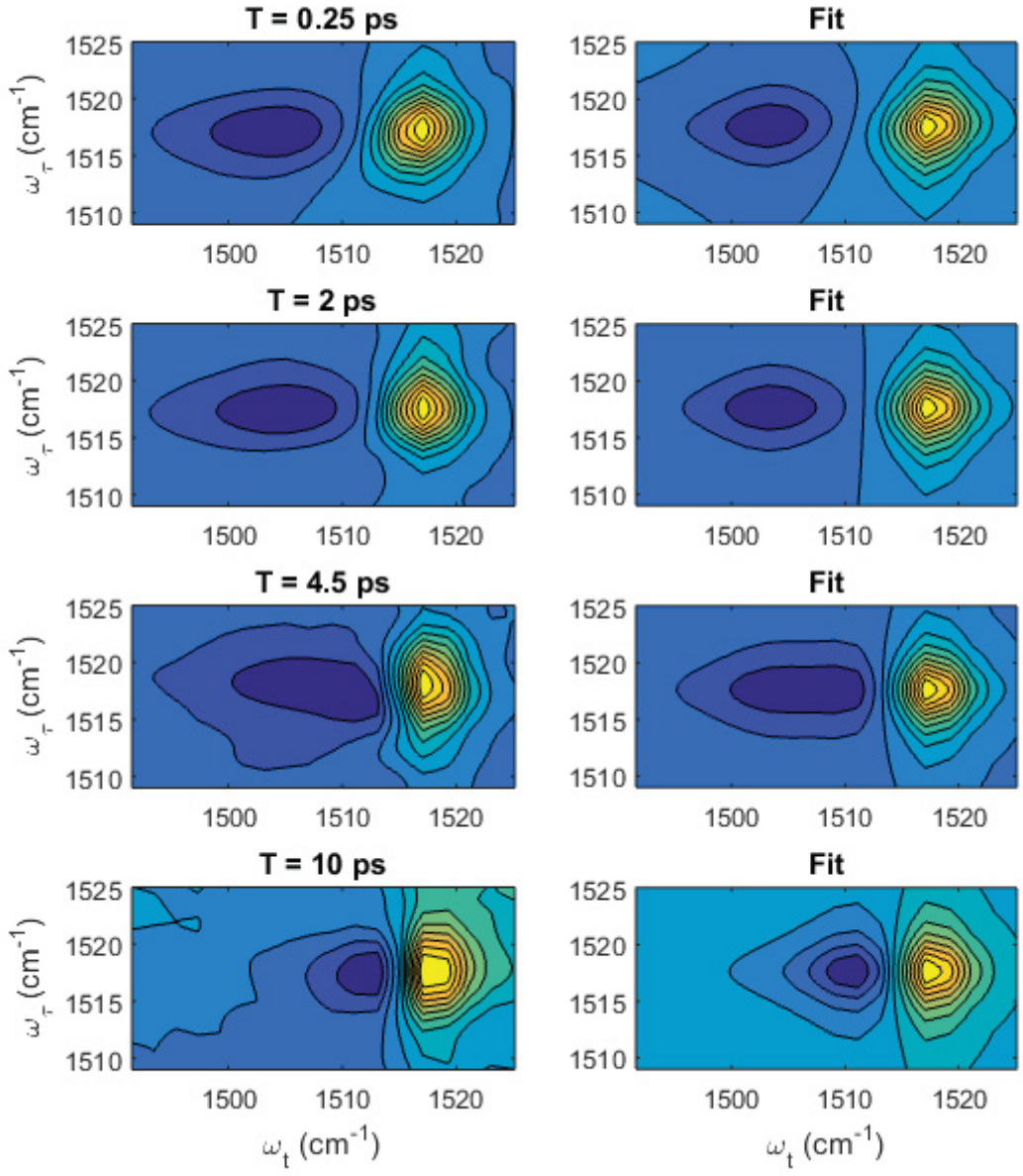

Figure S13. (Left) Experimental 2D IR spectra of Menk in pD 7 buffer and (right) response function fitting with the IVR model.

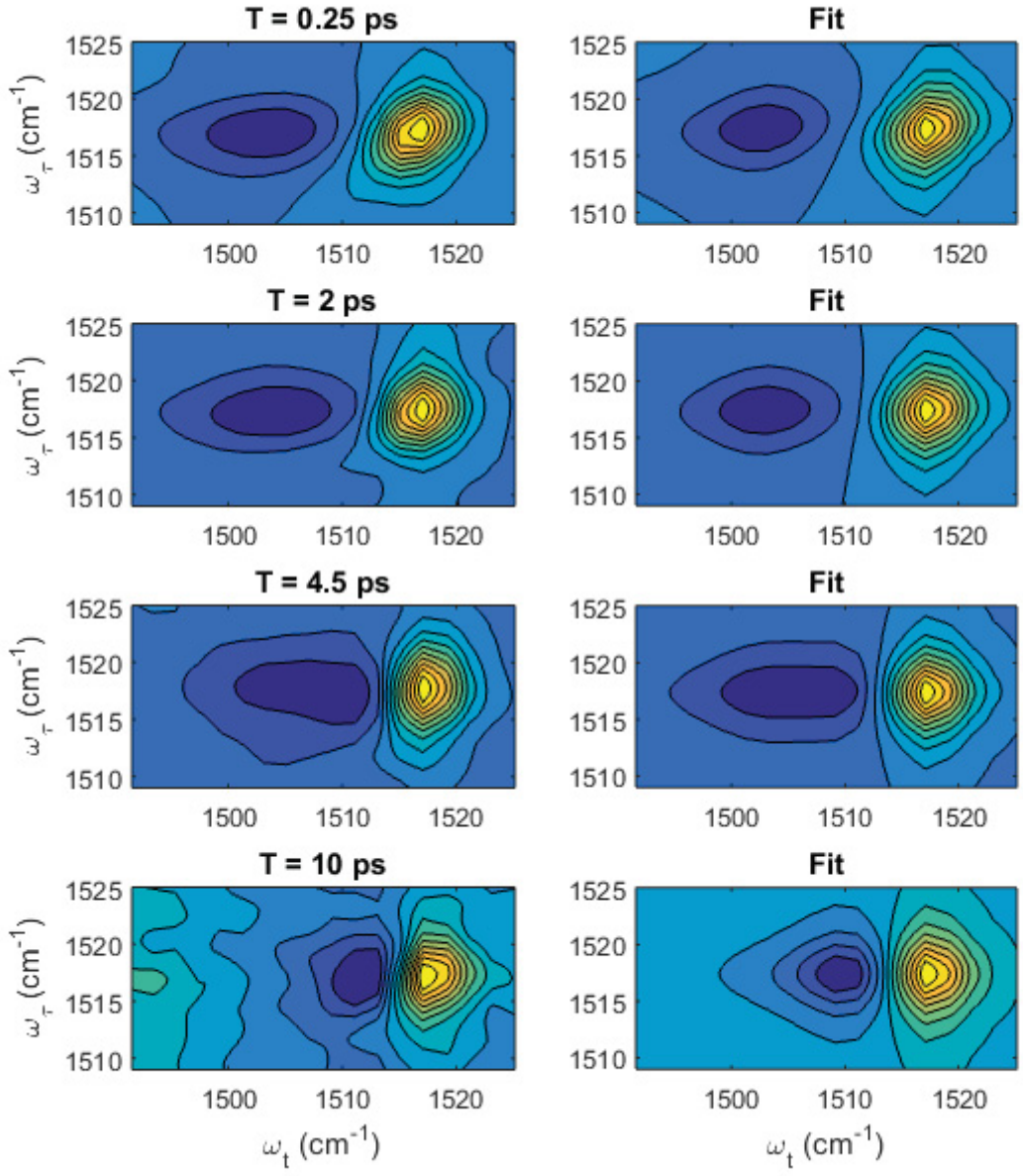

Figure S14. (Left) Experimental 2D IR spectra of Menk in PC bicelles and (right) response function fitting with the IVR model.

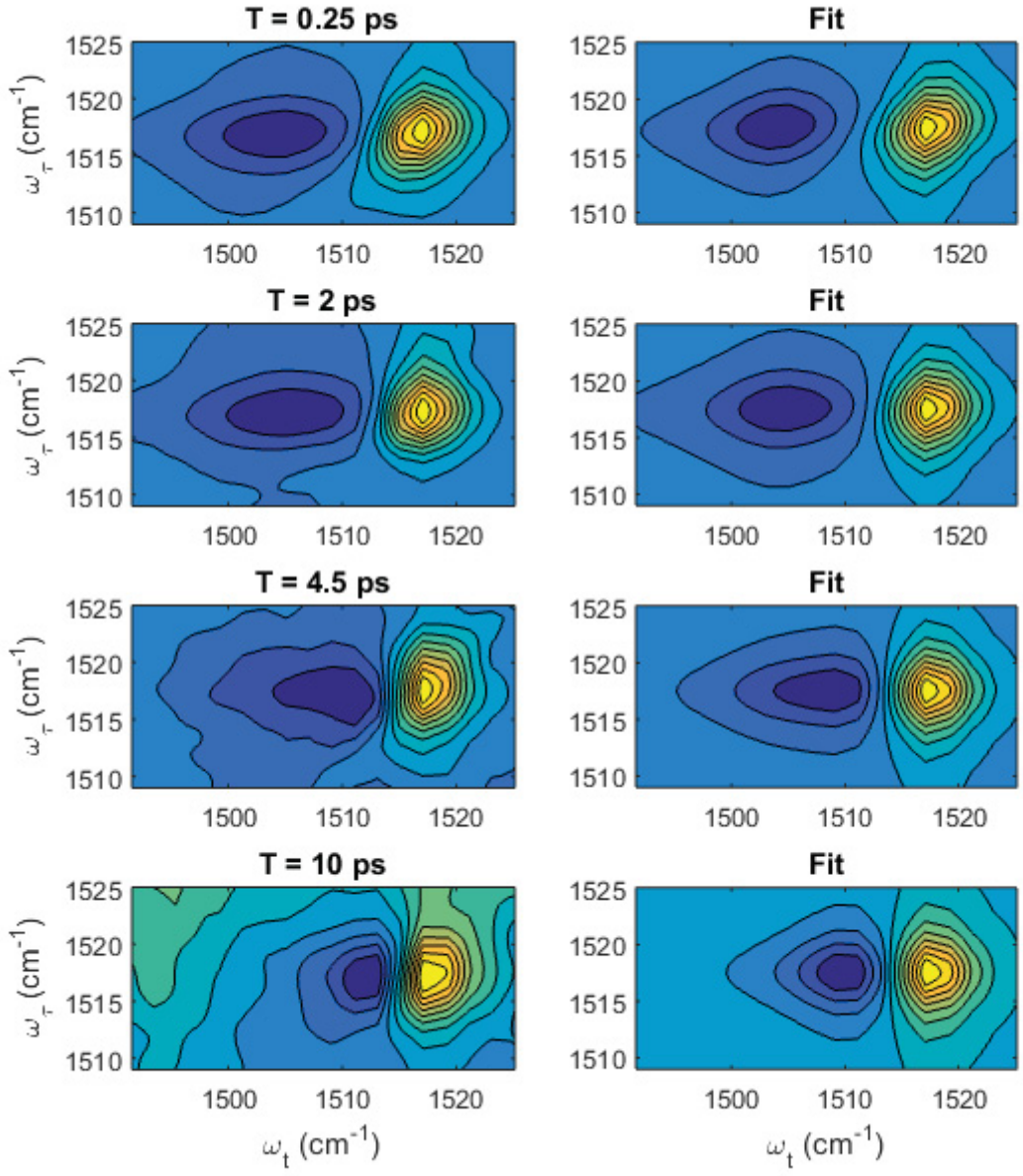

Figure S15. (Left) Experimental 2D IR spectra of Lenk in PE bicelles and (right) response function fitting with the IVR model.

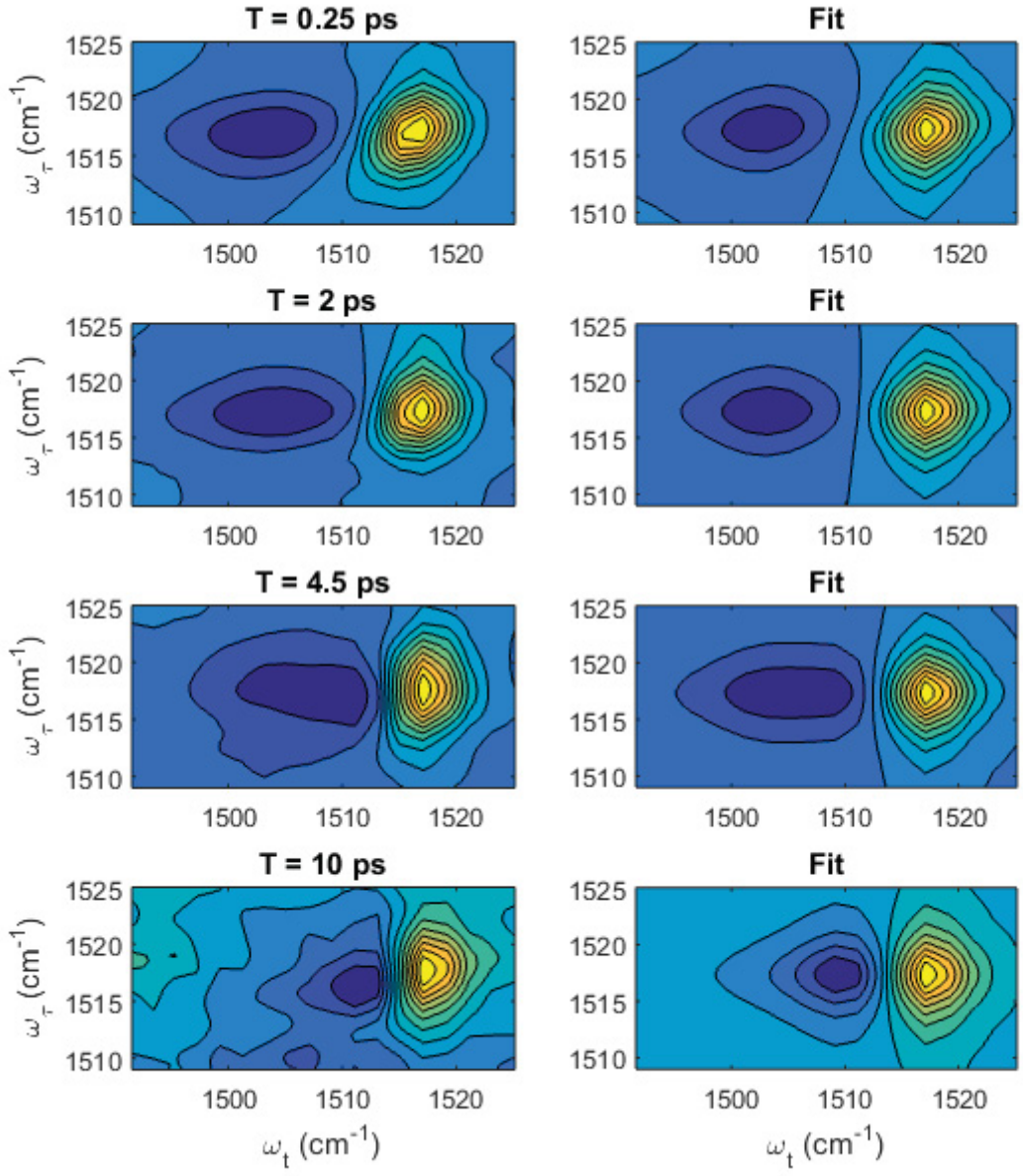

Figure S16. (Left) Experimental 2D IR spectra of Menk in PE bicelles and (right) response function fitting with the IVR model.

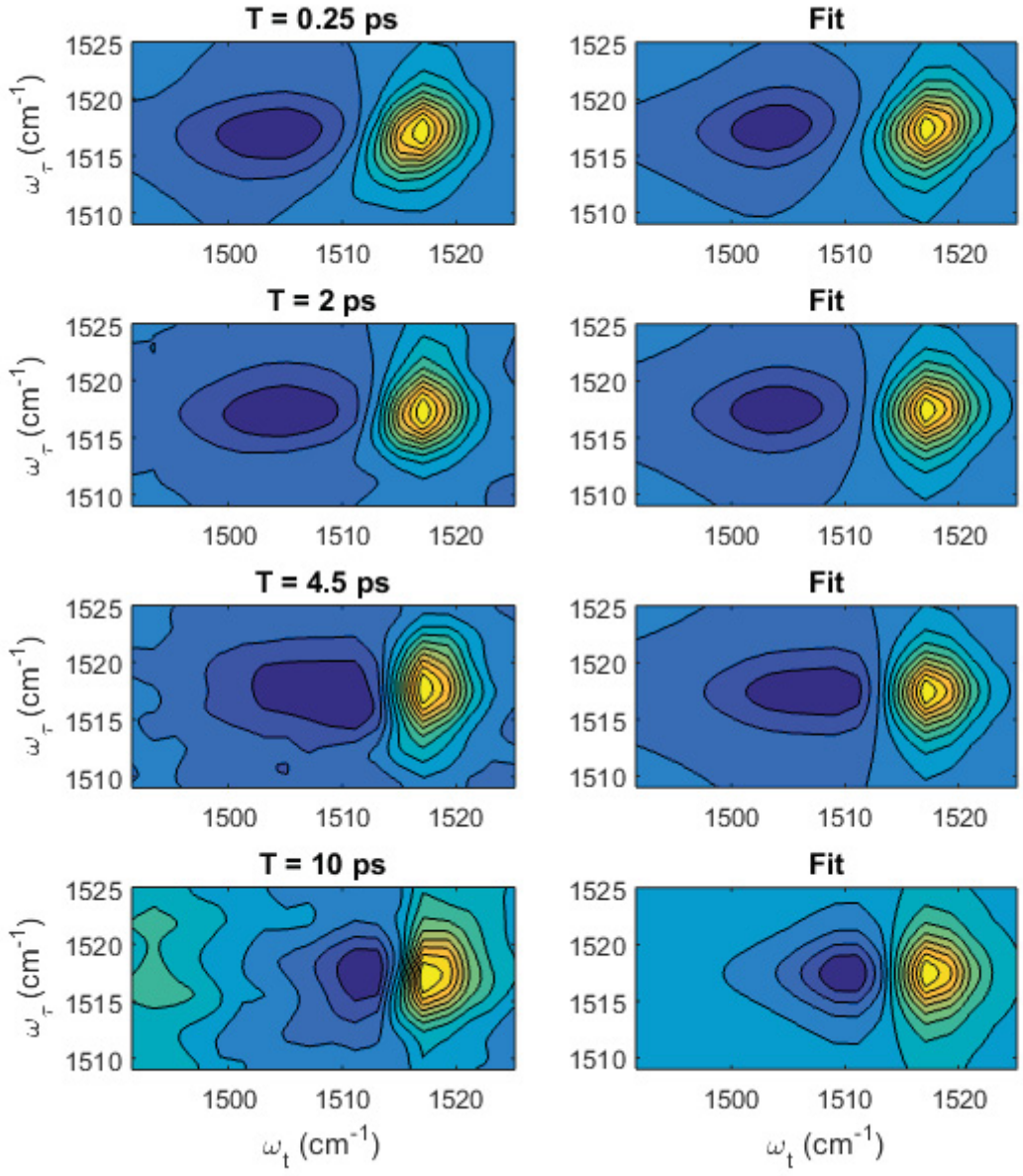

Figure S17. (Left) Experimental 2D IR spectra of Lenk in PG bicelles and (right) response function fitting with the IVR model.

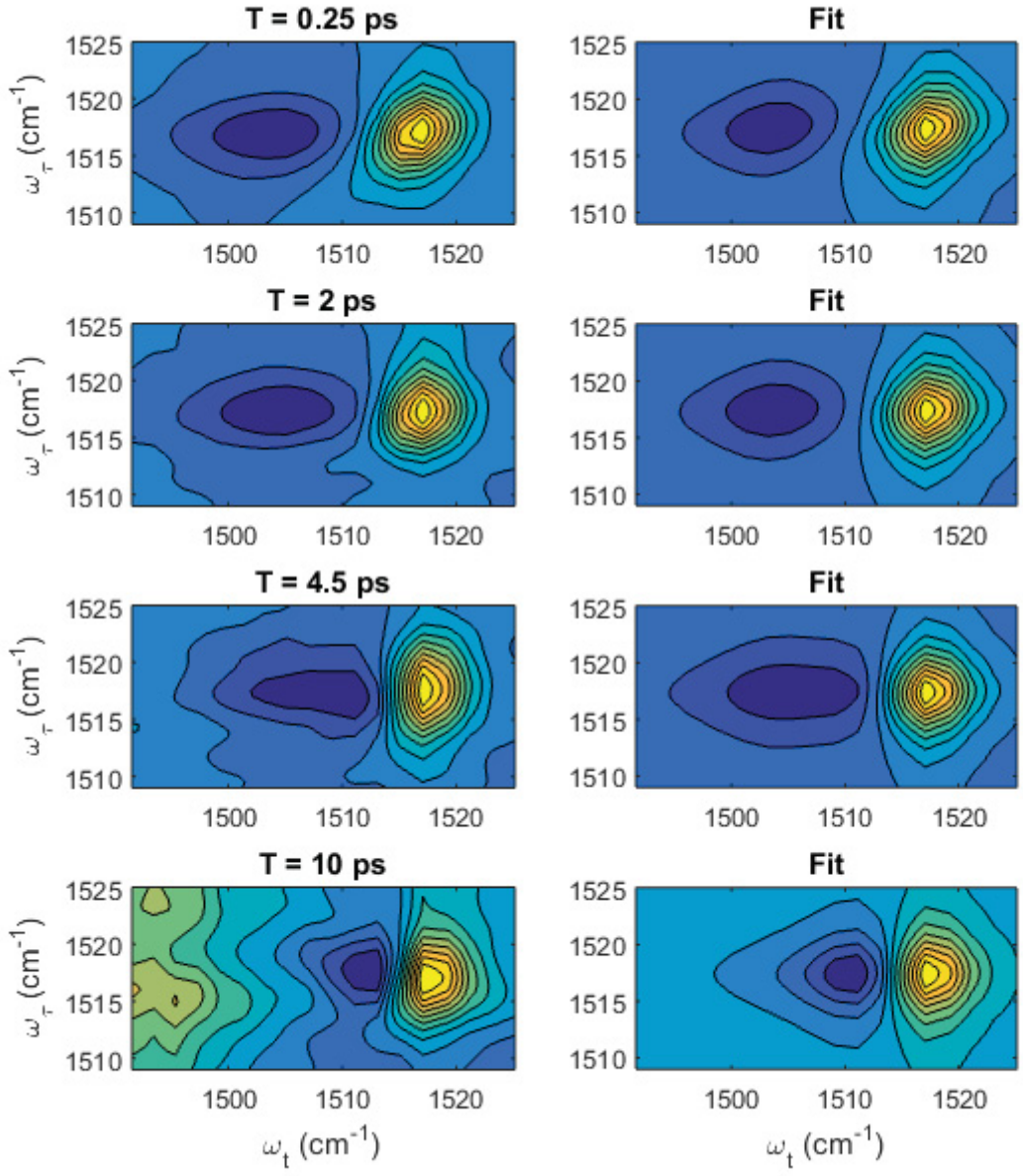

Figure S18. (Left) Experimental 2D IR spectra of Menk in PG bicelles and (right) response function fitting with the IVR model.

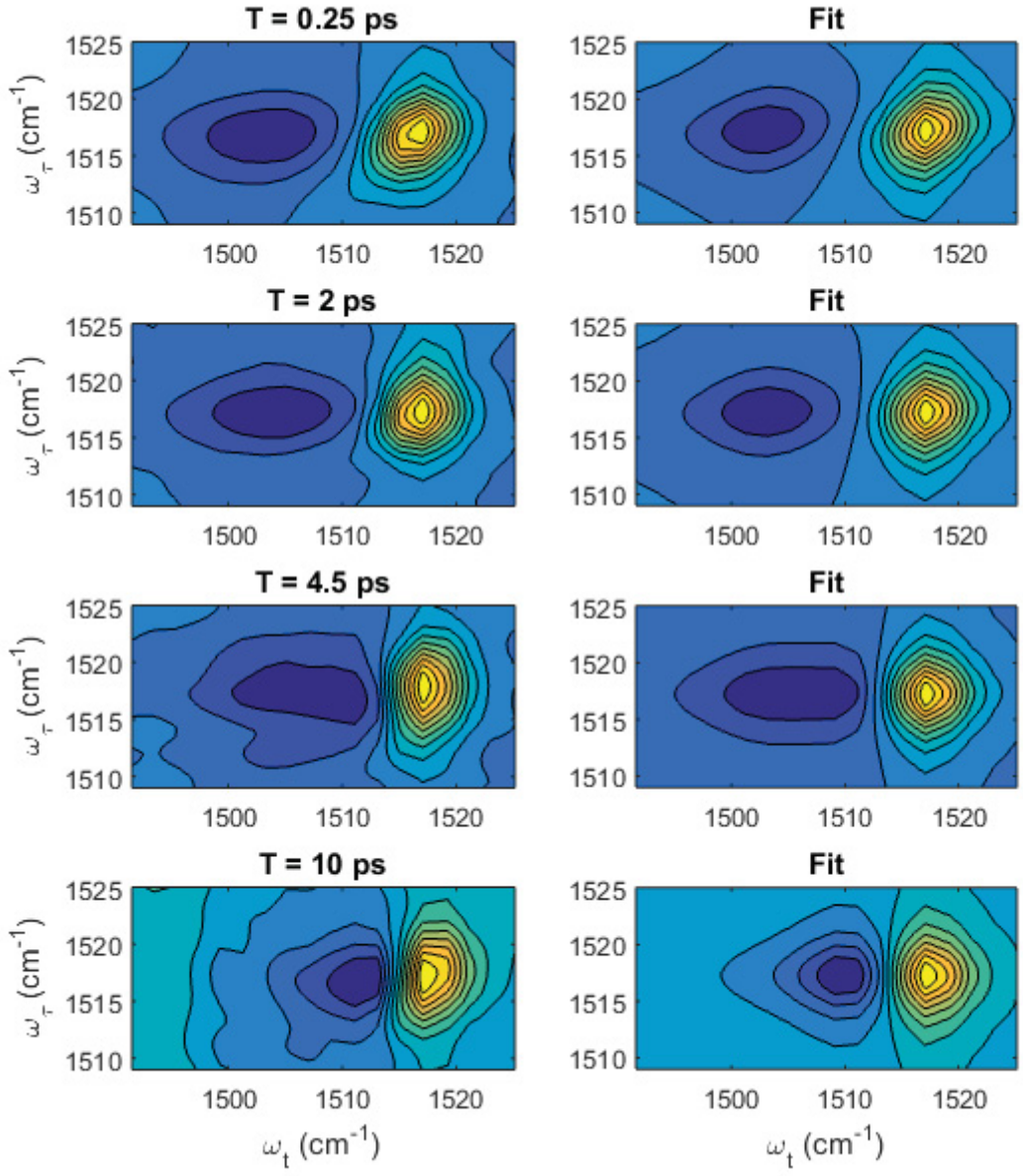

Figure S19. (Left) Experimental 2D IR spectra of Lenk in PS bicelles and (right) response function fitting with the IVR model.

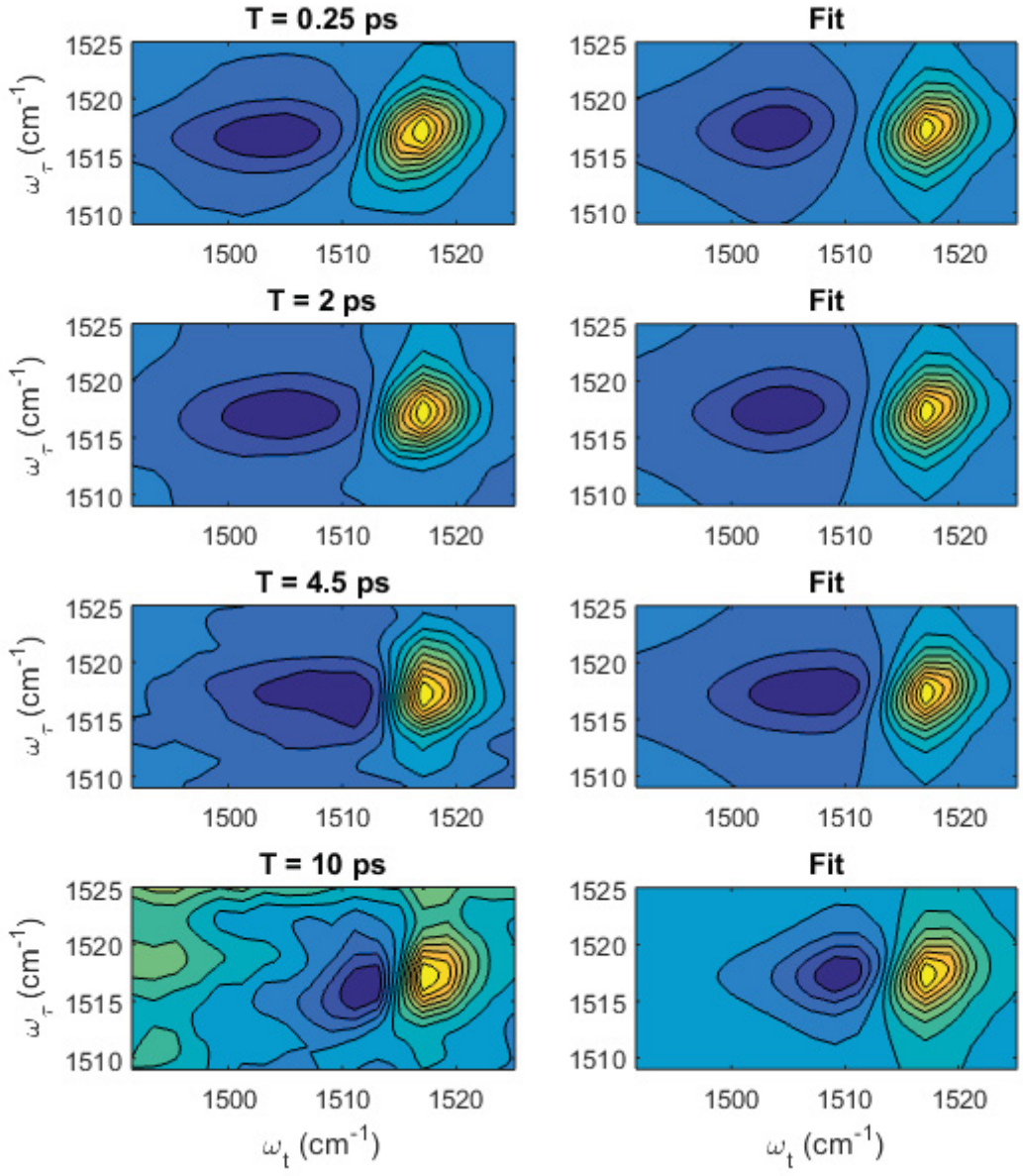

Figure S20. (Left) Experimental 2D IR spectra of Menk in PS bicelles and (right) response function fitting with the IVR model.

Table S4. Summary of 2D IR spectral fitting parameters with the response functions with IVR. Transition dipole moments, μ_{01} and μ_{12} are relative. Buffer refers to pD 7 buffer. Symbols are defined in the main text by Eq. 1 and Fig. 6.

	μ_{01}	μ_{12}	ω_{01} cm^{-1}	ω_{12} cm^{-1}	$\omega_{1',1+1'}$ cm^{-1}	T_1 ps	T_{IVR} ps	$T_{1'}$ ps	τ_1 ps	Δ_1 cm^{-1}	Δ_2 cm^{-1}	γ_0 cm^{-1}
p-Cresol/Buffer	0.28	0.25	1515.1	13.0	5.3	2.9	13.6	13.3	1.0	2.6	0	0.69
p-Cresol/DMSO	0.28	0.2	1516.7	16.9	5.7	3.0	3.6	15.2	1.1	1.9	0.27	1.84
Lenk/Buffer	0.25	0.22	1517.8	13.2	6.0	1.8	6.4	4.9	1.0	2.6	0	0.54
Lenk/PC	0.23	0.19	1517.5	14.0	6.7	1.8	9.0	5.8	2.1	2.4	0.16	0.20
Lenk/PE	0.23	0.20	1517.5	13.4	6.9	1.8	6.2	4.7	1.9	2.4	0	0.51
Lenk/PG	0.22	0.18	1517.4	13.7	6.5	1.8	9.6	6.3	1.8	2.5	0	0.07
Lenk/PS	0.22	0.18	1517.3	14.2	6.6	1.8	13	8.8	1.8	2.5	0.17	0.30
Menk/Buffer	0.25	0.21	1517.6	14.2	6.3	1.7	11.3	7.0	1.0	2.5	0.02	0.69
Menk/PC	0.23	0.19	1517.4	14.6	7.0	1.8	14.0	8.0	1.9	2.4	0.04	0.11
Menk/PE	0.23	0.19	1517.3	14.3	7.1	1.8	14.3	8.2	1.4	2.6	0	0.54
Menk/PG	0.21	0.16	1517.4	13.7	6.0	1.8	15.0	7.5	1.8	2.5	0.42	0.29
Menk/PS	0.2	0.17	1517.4	13.6	7.4	1.8	10.1	6.4	0	2.0	1.20	1.33

S7. 2D IR Spectra of p-Cresol in Hexanes

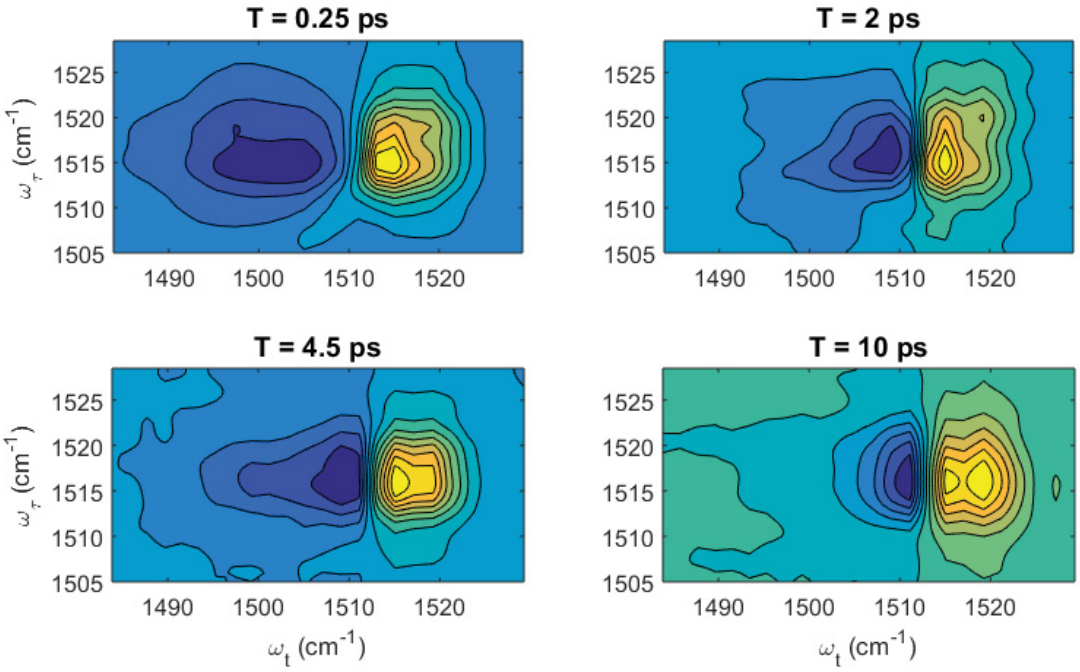

Figure S21: 2D IR Spectra of 40 mM p-cresol in hexanes. This series of 2D IR spectra exhibits line shape evolution that is typical for a coupled two-oscillator system, different from the line shape distortion observed for the single oscillator systems throughout this work.

S8. Line Shape Distortion in Lenk in pD 7 Buffer

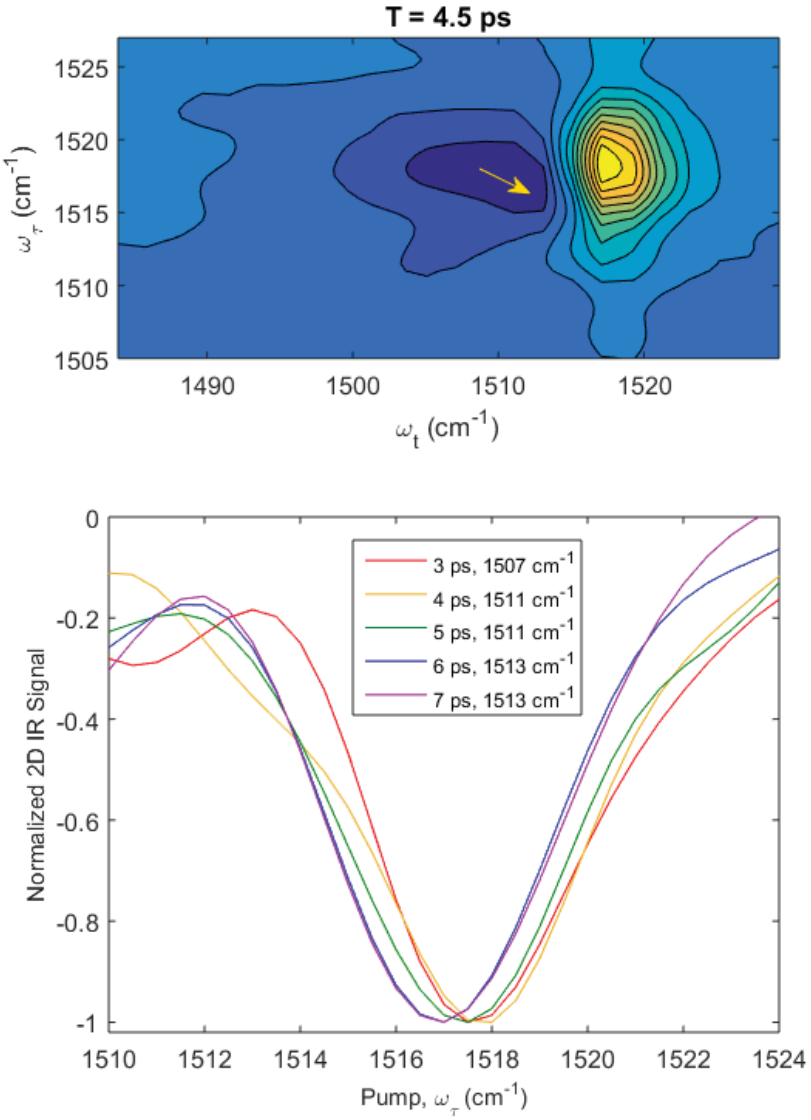

Figure S22: This figure illustrates the line shape distortion discussed in the main text. The top panel shows Lenk in pD 7 buffer at waiting time 4.5 ps, where the line shape distortion is most apparent. The apparent red shifting of the IVR peak is labeled with the golden arrow. The bottom panel provides slices along ω_τ at different waiting times as the $v = 1 \rightarrow 2$ peak appears to shift into the IVR peak. The slice was taken at the ω_t point that corresponds to the minimum in the 2D IR spectrum. This panel show how the interference between the two peaks red shifts with longer waiting time. The red shifting correlates with the dip seen in our CLS data.

S9. CLS Plots and Fitting Results

Figure S23 and Figure S24 summarize the CLS results. In Figure S23, we include error bars which estimate the CLS error. To calculate this error, we subdivided each 2D data set into 10 subsets and calculated the CLS for each subset. The error bars represent the standard deviation in the resulting set of CLS values. Each error also has a circle indicating the mean CLS point calculated from the subsets. The solid line represents the CLS extracted from the full data set. Note that for p-cresol the error bars are very large, even though the 2D IR data has a high SNR. This is because the width of the p-cresol peak is on the limit of our spectrometer's resolution. Therefore, the CLS value is extremely sensitive to small amounts of noise. For Lenk and Menk, the diagonal peak becomes narrower with longer waiting time (which is not predicted by the response function model). Therefore, the resolution problem is partially responsible for the large error bars at long waiting time, although the low SNR of the longer waiting times is the most important contributor.

In Figure S24, we present the CLS fits to the damped oscillation. Table S5 summarizes the full fitting parameters. We used the standard deviations shown in Figure S23 as standard error weights for the fitting. The fitting function is:

$$f(T) = {\Delta_1}^2 \cdot \cos\left(\frac{2\pi T}{\tau_1}\right) \cdot e^{-\frac{T}{\tau_2}} + {\Delta_2}^2 \qquad \text{(S2)}$$

Note that this fitting function does not represent a physical correlation function. Instead, it is an attempt to extract the static inhomogeneous contribution to the correlation function given the peak interference present in the 2D data. As such, some of the fits may not have physically meaningful results. For example, Lenk and Menk in pD 7 buffer have a slight negative static inhomogeneities within the error bars.

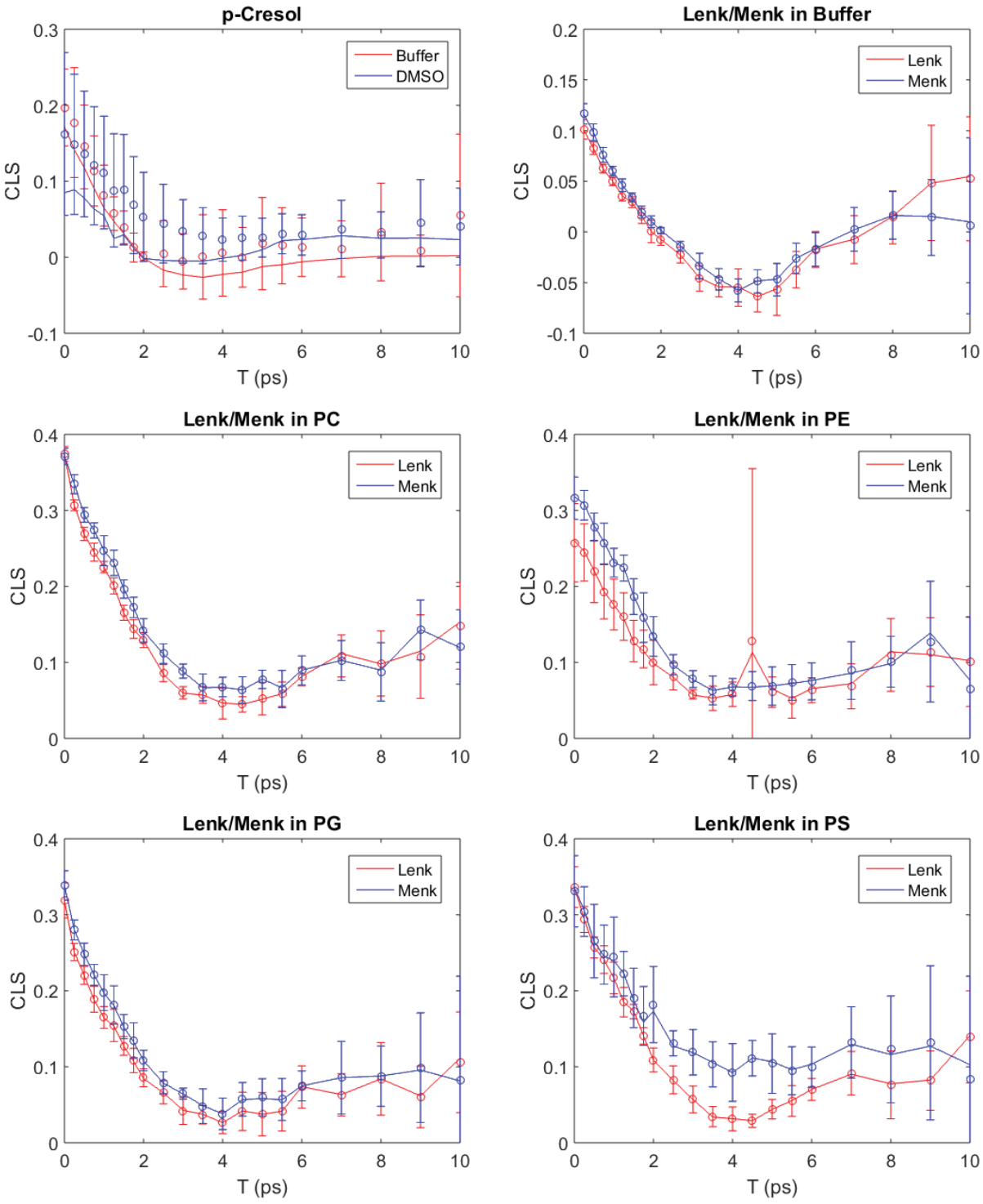

Figure S23. CLS results for all 2D data collected with the error bars shown.

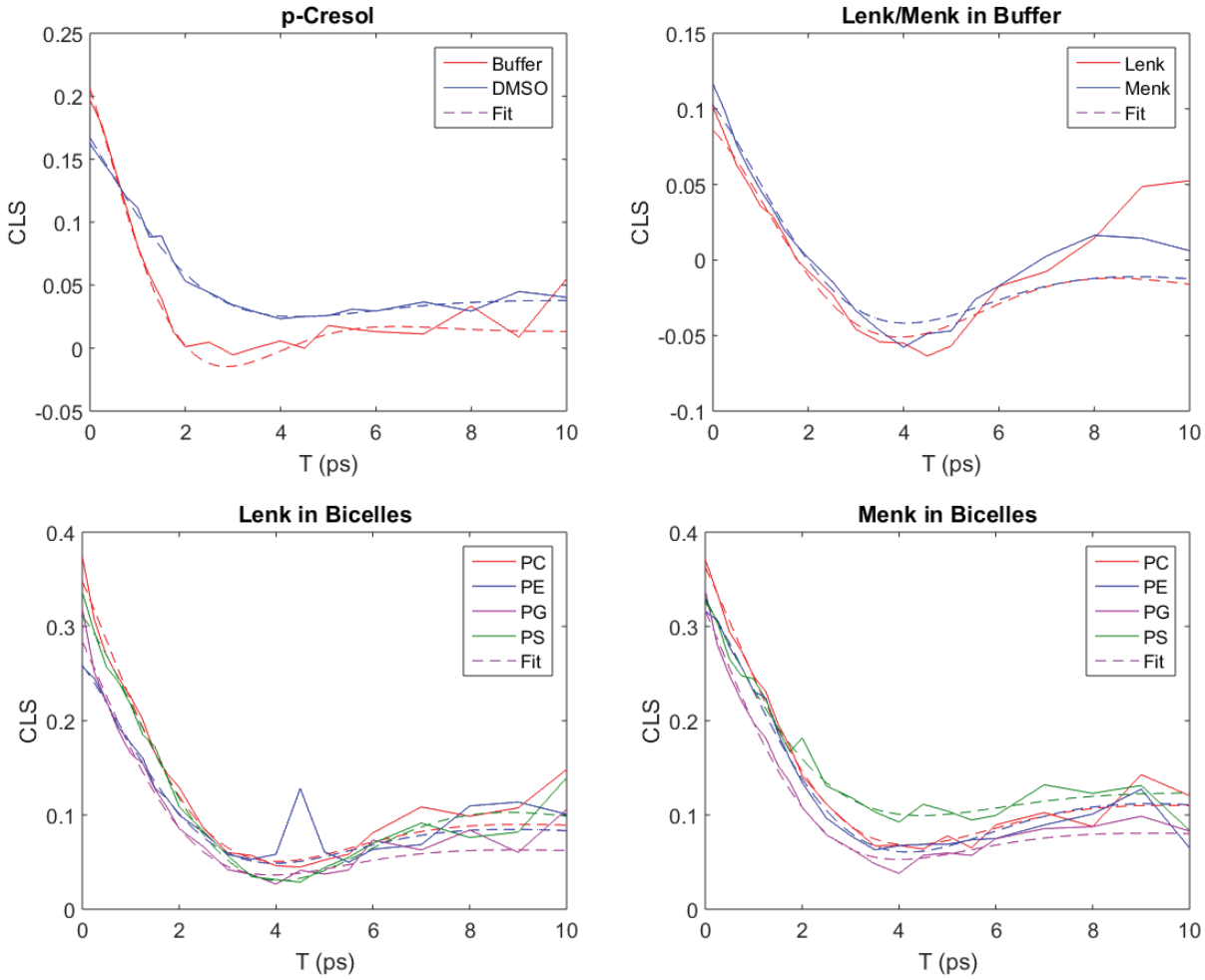

Figure S24. Plots of the CLS data and fitting results.

Table S5. CLS fitting parameters. Buffer refers to pD 7 buffer. The parameters are defined in Eq. S2 or Eq. 7 in the main text.

		Δ_1^2	Δ_2^2	τ_1	τ_2
p-Cresol	Buffer	0.19 ± 0.04	0.01 ± 0.01	7.1 ± 0.9	1.7 ± 0.7
	DMSO	0.13 ± 0.03	0.04 ± 0.01	11.3 ± 2.0	2.1 ± 0.7
Lenk	Buffer	0.11 ± 0.04	-0.02 ± 0.02	9.0 ± 2.7	3.4 ± 2.8
	PC	0.26 ± 0.06	0.09 ± 0.03	10.0 ± 3.2	2.2 ± 1.0
	PE	0.18 ± 0.05	0.08 ± 0.02	9.6 ± 1.4	2.5 ± 1.3
	PG	0.22 ± 0.05	0.06 ± 0.03	10.0 ± 3.5	2.0 ± 0.9
	PS	0.22 ± 0.04	0.09 ± 0.02	9.5 ± 1.1	3.3 ± 1.2
Menk	Buffer	0.12 ± 0.04	-0.02 ± 0.02	9.6 ± 3.1	2.9 ± 2.0
	PC	0.26 ± 0.03	0.11 ± 0.02	10.4 ± 2.0	2.4 ± 0.7
	PE	0.22 ± 0.04	0.10 ± 0.02	10.0 ± 1.6	2.8 ± 1.1
	PG	0.24 ± 0.04	0.08 ± 0.02	10.2 ± 2.5	2.0 ± 0.7
	PS	0.21 ± 0.05	0.12 ± 0.03	11.4 ± 4.0	2.3 ± 1.2

S10. Computational Detail for the Population Exchange with Hot-States Model

To calculate the response functions with an arbitrary kinetic model, we partition the problem into calculating the dephasing dynamics and calculating the population dynamics. The population dynamics are represented by a kinetic model, as described in the main text. When evaluated on a time grid, this method can be written in matrix notation:

$$\boldsymbol{R}(T) = \boldsymbol{G}(T) \circ \boldsymbol{Pr} \cdot \boldsymbol{M}(T) \cdot \boldsymbol{Pu} \tag{S3}$$

here, $\boldsymbol{R}(T)$ is the total rephasing or non-rephasing response function on a $N_t \times N_\tau$ time grid; $\boldsymbol{Pu}$ is a $N_{Pu} \times N_\tau$ matrix; $\boldsymbol{Pr}$ is a $N_t \times N_{Pr}$ matrix; $\boldsymbol{G}(T)$ is a matrix containing the exponential of the line shape function which is responsible for spectral diffusion; the $\cdot$ product represents matrix multiplication; and the $\circ$ product represents the Hadamard product, or by-element multiplication. The matrices $\boldsymbol{Pu}$ and $\boldsymbol{Pr}$ represent the first and second half of all rephasing or non-rephasing Feynman diagrams evaluated on the τ and t time grids, respectively. N_{Pu} and N_{Pr} represent the number of populations after the second and last interaction, respectively. N_τ and N_t represent the number of τ and t grid points used in the calculation. The matrix $\boldsymbol{M}(T) = \exp(\boldsymbol{K}T)$, of dimensionality $N_{Pr} \times N_{Pu}$, is the T-dependent solution to the linear kinetic equations for each pump-generated population, where $\boldsymbol{K}$ is the kinetic matrix of first order rate constants. As an example, the solution for the hot-band kinetic model is shown in Figure S25. Note that the rephasing and non-rephasing response functions need to be calculated separately. Finally, assuming the semi-impulsive limit, the spectra are Fourier transformed, for each time T, along (t, τ) to $(\omega_t, -\omega_\tau)$ for rephasing and $(\omega_t, +\omega_\tau)$ for non-rephasing response functions.[8] The absorptive spectra are the real parts of the sum of the rephasing and non-rephasing spectra.

The matrices $\boldsymbol{Pr}$ and $\boldsymbol{Pu}$ are constructed directly from the Feynman pathways. As an example, the rephasing equations that involve the 1st excited state as a population are given by:

$$\boldsymbol{Pu}^R_{i1} = -\mu_{01}^2 \cdot \exp\left(\tau_i\left(i\omega_{01} - \frac{1}{2T_1}\right)\right) \tag{S4}$$

$$\boldsymbol{Pr}^R_{1i} = \mu_{01}^2 \cdot \exp\left(t_i\left(-i\omega_{01} - \frac{1}{2T_1}\right)\right) - \mu_{12}^2 \cdot \exp\left(t_i\left(-i\omega_{12} - \frac{2}{3T_1}\right)\right) \tag{S5}$$

The indices i indicates the ith grid point on which the experimental times, t_i or τ_i, are evaluated on. The other index indicates the population (0 for ground state, 1 for excited state, etc.) and

corresponds to a row or column in the matrices. The diagrams that involve the ground state are given by:

$$\boldsymbol{Pu}_{i0}^{R} = -\mu_{01}^{2} \cdot \exp\left(\tau_i\left(i\omega_{01} - \frac{1}{2T_1}\right)\right) \tag{S6}$$

$$\boldsymbol{Pr}_{0i}^{R} = \mu_{01}^{2} \cdot \exp\left(t_i\left(-i\omega_{01} - \frac{1}{2T_1}\right)\right) \tag{S7}$$

There is an additional probe pulse term involving the IVR peak:

$$\boldsymbol{Pr}_{1'i}^{R} = -\mu_{1,1+1'}^{2} \cdot \exp\left(t_i\left(-i\omega_{1,1+1'} - \frac{1}{2T_{1'}} - \frac{1}{T_1}\right)\right) \tag{S8}$$

The spectral diffusion component, $\boldsymbol{G}(T)$, is given in the usual way:[9]

$$\boldsymbol{G}_{ij}^{R}(T) = \exp\left(-g(\tau_j) + g(T) - g(t_i) - g(\tau_j + T) - g(t_i + T) + g(\tau_j + T + t_i)\right) \tag{S9}$$

$$\boldsymbol{G}_{ij}^{NR}(T) = \exp\left(-g(\tau_j) - g(T) - g(t_i) + g(\tau_j + T) + g(t_i + T) - g(\tau_j + T + t_i)\right) \tag{S10}$$

$$g(t) = \int_0^t dt_1 \int_0^{t_1} dt_2 C(t_2) \tag{S11}$$

where $C(t)$ is the FFCF, and indices i and j indicates the i and j^{th} grid-point on which t and τ are defined on. Finally, when there is no spectral diffusion, this calculation can be directly performed in the frequency domain.

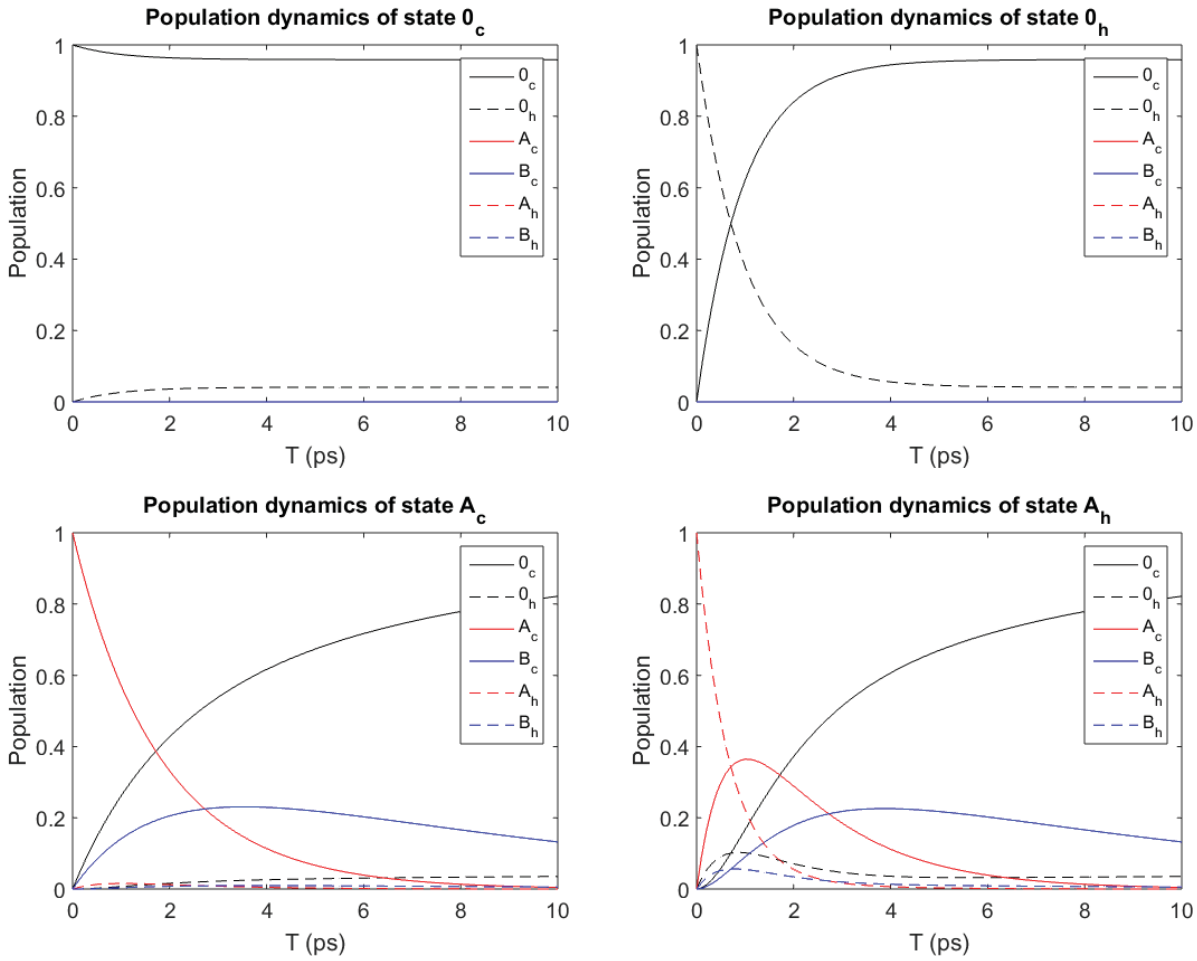

Figure S25. The population dynamics represented by the population transfer matrix for the hot-states exchange model.

References

1. Y. Feng, I. Vinogradov, and N.-H. Ge, "Optimized noise reduction scheme for heterodyne spectroscopy using array detectors," *Opt. Express* **27**, 20323 (2019).
2. Y. Feng, I. Vinogradov, and N.-H. Ge, "General noise suppression scheme with reference detection in heterodyne nonlinear spectroscopy," *Opt. Express* **25**, 26262 (2017).
3. S.-H. Shim and M. T. Zanni, "How to turn your pump–probe instrument into a multidimensional spectrometer: 2D IR and Vis spectroscopiesvia pulse shaping," *Phys. Chem. Chem. Phys.* **11**, 748 (2009).
4. H.-S. Tan, I. R. Piletic, and M. D. Fayer, "Polarization selective spectroscopy experiments: methodology and pitfalls," *Journal of the Optical Society of America B* **22**, 2009 (2005).
5. F. Chalyavi, D. G. Hogle, and M. J. Tucker, "Tyrosine as a Non-perturbing Site-Specific Vibrational Reporter for Protein Dynamics," *J. Phys. Chem. B* **121**, 6380 (2017).
6. M. J. Frisch, G. W. Trucks, H. B. Schlegel, G. E. Scuseria, M. A. Robb, J. R. Cheeseman, J. A. Montgomery, T. Vreven, K. N. Kudin, J. C. Burant, J. M. Millam, S. S. Iyengar, J. Tomasi, V. Barone, B. Mennucci, M. Cossi, G. Scalmani, N. Rega, G. A. Petersson, H. Nakatsuji, M. Hada, M. Ehara, K. Toyota, R. Fukuda, J. Hasegawa, M. Ishida, T. Nakajima, Y. Honda, O. Kitao, H. Nakai, M. Klene, X. Li, J. E. Knox, H. P. Hratchian, J. B. Cross, V. Bakken, C. Adamo, J. Jaramillo, R. Gomperts, R. E. Stratmann, O. Yazyev, A. J. Austin, R. Cammi, C. Pomelli, J. W. Ochterski, P. Y. Ayala, K. Morokuma, G. A. Voth, P. Salvador, J. J. Dannenberg, V. G. Zakrzewski, S. Dapprich, A. D. Daniels, M. C. Strain, O. Farkas, D. K. Malick, A. D. Rabuck, K. Raghavachari, J. B. Foresman, J. V. Ortiz, Q. Cui, A. G. Baboul, S. Clifford, J. Cioslowski, B. B. Stefanov, G. Liu, A. Liashenko, P. Piskorz, I. Komaromi, R. L. Martin, D. J. Fox, T. Keith, A. Laham, C. Y. Peng, A. Nanayakkara, M. Challacombe, P. M. W. Gill, B. Johnson, W. Chen, M. W. Wong, C. Gonzalez, and J. A. Pople. Gaussian 03, Revision C.01, 2003.
7. C. T. Middleton, A. M. Woys, S. S. Mukherjee, and M. T. Zanni, "Residue-specific structural kinetics of proteins through the union of isotope labeling, mid-IR pulse shaping, and coherent 2D IR spectroscopy," *Methods* **52**, 12 (2010).
8. N.-H. Ge and R. M. Hochstrasser, "Femtosecond two-dimensional infrared spectroscopy: IR-COSY and THIRSTY," *PhysChemComm* **5**, 17 (2002).
9. P. Hamm and M. Zanni. *Concepts and Methods of 2D Infrared Spectroscopy*; Cambridge University Press: Cambridge, 2011.